PONTIFICIA UNIVERSIDAD CATOLICA DE CHILE
SCHOOL OF ENGINEERING

AERODYNAMIC AND GEOMETRIC CHARACTERIZATIONS FOR FOG COLLECTING MESHES

FÉLIX ECHEVARRÍA JOHNSON

Thesis submitted to the Office of Research and Graduate Studies
in partial fulfillment of the requirements for the degree of
Master of Science in Engineering

Advisor:
JUAN DE DIOS RIVERA AGUERO

Santiago de Chile, December 2015

PONTIFICIA UNIVERSIDAD CATOLICA DE CHILE
SCHOOL OF ENGINEERING

AERODYNAMIC AND GEOMETRIC CHARACTERIZATIONS FOR FOG COLLECTING MESHES

FÉLIX ECHEVARRÍA JOHNSON

Members of the Committee:
JUAN DE DIOS RIVERA AGUERO
WOLFRAM JAHN VON ARNSWALDT
JACQUES DUMAIS
JOSE LUIS ALMAZAN CAMPILLAY

Thesis submitted to the Office of Research and Graduate Studies
in partial fulfillment of the requirements for the degree of
Master of Science in Engineering

Santiago de Chile, December 2015

Gratefully to my family

ACKNOWLEDGEMENTS

I would like to thank the following people for their collaborations/contributions: Juan de Dios Rivera, Maria Tou, Jorge Gomez, Sebastián Fehrmann, Luis Valdés, Marcelo Gutierrez, Geert Geisterfer.

TABLE OF CONTENTS

LIST OF FIGURES

LIST OF TABLES

ABSTRACT

The Aerodynamic collection efficiency (ACE) of a fog water collector (FWC) depends mainly on the two-dimensional solidity and the pressure loss coefficient (C_0) of the selected mesh.

The two dimensional solidity can be accurately measured by using a digital image analysis with ImageJ software (free online source). The method that we developed consists of taking a photo of the mesh and converting it into a binary black and white pixel image so as to calculate the solidity based on the ratio of black to white pixels. The pressure loss coefficient was calculated using a wind tunnel that measured both the pressure loss of the air after passing through the mesh and the upstream wind velocity.

Ultimatly, a characterization of two types of meshes was done in order to get the pressure loss coefficient as a function of the two dimensional solidity for each variety of mesh. Our Results show that round filament meshes have a lower C_0 for the same solidity than ribbon filament meshes. Thus, the maximum theoretical aerodynamic collection efficiency of the ribbon type mesh is 0.2102 at a solidity of 0.502 while round filament meshes can reach to an ACE of 0.263 at a solidity of 0.68. Since round filament meshes have thiner filament than ribbon meshes, it also has a better deposition efficiency. Thus the maximum total collection efficiency of a round type can be 123 % higher than a ribbon type at a wind velocity of 2 ms^{-1}. For wind velocities of 10 ms^{-1}, the total collection efficiency of a round filament mesh is up to 36 % higher than a ribbon filament mesh.

Keywords: fog water collector, mesh, two-dimensional solidity, porosity, pressure drop, aerodynamics, porous media, .

RESUMEN

La eficiencia aerodinámica de colección de un atrapanieblas depende principalmente de la solidez bidimensional y el coeficiente de caída de presión (C_0) de la malla.

La solidez bidimensional puede ser medida de manera precisa usando anális de imagenes digitales con el software ImageJ (descarga gratuita). El método consiste en tomar una fotografía de la malla y convertirla en una imagen binaria de pixeles blancos y negros. Luego, la solidez es calculada según la proporción de los pixeles. El coeficiente de caída de presión fue medido con un túnel de viento capaz de medir la caída de presión a través de la malla y la velocidad del viento aguas arriba de esta.

Finalmente, se hizo una caracterización de dos tipos de malla para obtener el coeficiente de caída de presión en función de la solidez bidimensional. Los resultados muestran que las mallas con filamentos redondos tienen un menor C_0 para una misma solidez que las mallas de filamentos de cinta. Así la máxima eficiencia aerodinámica teórica de una malla con filamentos de cinta es 0.2102 a una solidez de 0.502, mientras que las mallas con filamentos redondos pueden alcanzar 0.263 a una solidez de 0.68.

Debido a que las mallas de filamento redondo tienen filamentos más delgados que las tipo cinta, tienen también mejor eficiencia de deposición. Así, la máxima eficiencia total de colección de una malla de filamento redondo puede ser un 123% mayor que una malla de filamento tipo cinta para velocidades de viento de 2 ms^{-1}. Para velocidades de 10 ms^{-1}, la eficiencia total de colección de una malla de filamento redondo es un 36% mayor que la de una malla de filamento tipo cinta.

Palabras Claves: atrapanieblas, malla, solidez bidimensional, porosidad, caída de presión, aerodinámica, medios porosos.

1. INTRODUCTION

Fog water collectors (FWC) have been used for decades in arid zones to collect fresh water in many countries of the world. The main factor that affects collection yields is the presence of periodic fog and the liquid water flux of it, which is measaured in $gm^{-2}s^{-1}$. FWC accumulate water by the interception of droplets through a mesh design, where the wind is an important factor in collection yields. For this reason, FWC projects have been normally situated near the west coast of continents, at a close proximity of the sea that provides a major source of humidity and a constant wind source that flows from west to east.

In addition to fog and wind factors, the mesh of the FWC plays an important role in the efficiency of the collector. Different meshes may have different yields for the same conditions, which implies that the critical parameters can be identyfied in order to optimize the mesh and get more liters per square meter of mesh in a day ($L/m^2/day$). To identify these parameters it is necessary to understand the fog behavior when it passes through the mesh. Rivera (2011) studied the collection efficiency of FWC and proposed that since the FWC is an obstacle for the flow of driven fog, a part of the unperturbed flow passes around the mesh. That portion that flows through, only a fraction of the fog actually reaches the collector because part of this portion flows through the mesh holes following the airstream that flows around the fibers. Finally, some of the last portion that would reach the gutter is lost by re-entrainment and spill. Taking these losses into consideration, Rivera (2011) defined the collection efficiency as a product of three efficiencies:

$$\eta_{coll} = \eta_{AC}\eta_d\eta_{dr} \tag{1.1}$$

where η_{AC} is the aerodynamic collection efficiency, η_d is the deposition efficiency and η_{dr} is the draining efficiency, in the same order in which they were appointed.

This work is focused on improving η_{AC} which is defined by Rivera (2011) as

$$\eta_{AC} = \frac{\varsigma}{1 + \sqrt{\frac{C_0}{C_d}}} \tag{1.2}$$

where ς is the two dimensional solidity or ”solidity” of the mesh, defined as the relationship between the surface area of the threads and that of the total mesh; C_0 is the pressure loss coefficient and it depends on solidity; and C_d is the drag coefficient of a non-permeable screen and, therefore, is independent of solidity.

The objective of this work is to characterize meshes for FWC in terms of ς and C_0. A method to measure the solidity of meshes has been developed on chapter 2 and the pressure loss coefficient of meshes is determined on chapter 3. The following section will described in general terms what was achieved for each parameter.

1.1. Solidity

Solidity is a concept that represents the fraction of the surface covered by the mesh that is capable of collecting droplets. Most papers on fog collection use the concept ”shade coefficient” instead of the term solidity (Park, Chhatre, Srinivasan, Cohen, & McKinley,2013;Rivera,2011;Schemenauer & Joe,1989), but shade coefficient is measured by manufacturers which use a luxmeter, and consists of a light source that emits luxes through the mesh. The shade coefficient is calculated as a ratio between luxmeter measurements with and without the net sample (Castellano et al.,2008). The problem of this method is that a proportion of meshes used in FWC are made of a semi transparent material which allows light to pass through the filaments of mesh, while the concept of fog collecting does not depend on the transparency of the material. For this reason, we propose to use the term solidity instead of shade coefficient. Solidity is the complement of porosity, which has been used in several papers in the characterization of antiinsect nets in order to improve greenhouse ventilation (Valera, Alvarez, & Molina,2006; Bailey et al.,2003; Miguel, Braak, & Bot,1997; Teitel, Dvorkin, Haim, Tanny, & Seginer,2009). The problem of this parameter is that apparently their is no consensus on how to measure it. Some authors use geometric methods which provide fit results with woven type mesh, but most examples of mesh used in FWC are knitted and present a high variable shape content which depends on the region and structure of the design. This factor can be even more unpredictable in a double layer plan, which is very common for fog harvesting. Other authors use radiation balance, which conveys quality results for opaque meshes, but does not perform well with a transparent material. Therefore we developed the measurment technique of solidity as a way to measure a mesh based on a processed digital image of the mesh and then converting the image into a binary black and white code where black pixels corresponde to the mesh material and white pixels corresponde to the gaps. The solidity parameter is calculated as the ratio between the black pixels and the total amount of pixels.

Since the main objective of this method is to obtain a clear-cut image of the mesh with a well defined silhouette, reflective and light color meshes need to be photographied against a dark background. On the otherhand opaque and dark color meshes need to be photographied on a light table. The result of this method is a histogram that represents the distribution frecuency of greyscale in an 8 bit image that ranges between 0 (black) to 255 (white). Thus, a threshold value between 0 and 255 is chosen in order to assign the black level to those pixels below the threshold value and the white level to those above. The software used for this motive was ImageJ which has an algorithm that automatically selects the threshold value, neverthless at times it is necessary to set the threshold manually.

Due to the fact that the meshes tested have an unknown solidity, it is difficult to estimate an error of measurement with this method. To this purpose, digital meshes, with controlled solidity, were drawn on computer and printed. Applying the solidity method to the printed mesh examples, the measurement error was about 1% for meshes with a filament width of 3 mm and up to 3% for filaments with a width of 1 mm.

The most common used mesh in FWC is Raschel, which is made of knitted flat ribbon filaments of polyethylene. Usually FWC in Chile uses a double layer of 35 % shade coefficient Raschel mesh. The goal was to compare the 35% shade coefficient with the solidity calculated method. Results show that the solidity of a 35%SCRaschel was 0.47 which is 34% higher than the 0.35 assumed by fog harvesting studies.

1.2. Pressure loss coefficient

The pressure loss coefficient (C_0) of the mesh is directly related to the fraction of the unperturbed fog that is deviated and passes around and through the mesh. Indeed a high pressure loss coefficient implies that a large part of the flow will pass around the FWC. The pressure loss coefficient for different meshes has been studied by several authors. Idel'cik (1960) proposed correlations of C_0 for silk and wire meshes as a function of solidity, nevertheless knitted meshes such as Raschel mesh have not yet been studied.

To measure C_0 we designed and built a wind tunnel with a square section of 0.4 m x 0.4 m and 2.4 m long. The wind tunnel vary's the wind velocity from 0 to 8 ms^{-1} and is equipped with two differential pressure sensors (DPS) to measure upstream wind speed and pressure drop across the mesh.

For turbulent flow, when viscous forces do not dominate, pressure drop across the mesh can be calulated as

$$\Delta P = \frac{C_0 \rho u^2}{2} \tag{1.3}$$

The pressure drop and wind velocity was measured for each mesh at different wind velocities. The pressure loss coefficient can be calulated fiting a polinomyal of the form

$$\Delta P = au^2 \tag{1.4}$$

Then, C_0 is defined as

$$C_0 = \frac{2a}{\rho} \tag{1.5}$$

The fitted polynomial showed coefficients of determination over 0.99, which implies that the flow is dominated by inercial forces. If the curve that best fits to the data were linear, it would mean that the viscous forces dominate the flow.

Meshes that were tested, clasified in to two main groups depending on the filament shape: round filament type and ribbon filament type. The goal was to compare both types of filaments based on the concept of solidity and pressure loss coefficient to evaluate the aerodynamic collection efficiency of each family of meshes. The ribbon filament type data fitted to an exponencial function:

$$C_0 = 0.0744e^{6.85\varsigma} \tag{1.6}$$

while the relationship for round filament type meshes was:

$$C_0 = 0.1192e^{4.7526\varsigma} \tag{1.7}$$

Evaluating the aerodynamic collection efficiency for both examples, we can see that the ribbon filament meshes can reach a maximum of $\eta_{AC} = 0.2102$ at a solidity of 0.503, while round filament meshes can reach a maximum of $\eta_{AC} = 0.263$ at a solidity of 0.68.

On the other hand, Park et al. (2013) studied that deposition efficiency concludes that the critical parameters that affect this efficiency is the wind velocity, the droplet diameter and the filament width. Thus, deposition efficiency can be increased when the filament width is of the order of the droplet diameter which ranges between 0 and 20 μm (Schemenauer & Joe,1989). Due to the small values of the droplet diameters, the filament width needs to be as thin as possible in order to increase deposition efficiency. Indeed, round type meshes have smaller filament width than ribbon type meshes, which implies that round filament meshes not only have better aerodynamic collection efficiency, but also a better deposition efficiency.

Finally, considering a draining efficiency equal to 1, a collection efficiency of a ribbon filament mesh at 2 ms^{-1} is 0.098 and at the same wind speed for round filament type is 0.219. At wind velocities of 10 ms^{-1}, the collection efficiency of ribbon and round filament were 0.19 and 0.259 respectively.

2. AN IMAGE ANALYSIS METHOD FOR MEASURING TWO-DIMENSIONAL SOLIDITY OF MESHES

2.1. Introduction

Meshes are characterized by different structural features, radiometric properties, and physical and mechanical properties. Structural features include type of material, type and dimensions of fibers, texture, mesh size, porosity/solidity, and weight. Radiometric properties include color, transmissivity/ reflectivity/ shade coefficient. Relevant physical and mechanical properties are permeability, tensile strength and modulus of elasticity (Castellano & Russo,2005). Meshes have been used in many fields, but probably most extensively in agriculture. In this field, properties of mesh has been widely studied for its use as protection from hail, wind, snow, or strong rainfall in fruit-farming and ornamentals, shading nets for greenhouses and protection against virus-vector insects and birds (Castellano et al.,2008). Castellano also argued that in many cases different mesh types were adopted for the same application and the same cultivations methods by various growers. Results show that many end-users do not understand the relationship between the mesh optimization for a specific application and the construction parameters of the mesh. The choice often depends on empirical criteria and not on scientific and economic considerations.

In this context, fog water harvesting is another field that requires the study of mesh behavior in order to minimize the cost of fog collection. The solidity of the mesh, which is the ratio between the solid surface and the projected surface of the screen (the complement of porosity), has been identified as a critical parameter in determining the efficiency of the fog collector because it affects the pressure drop across the mesh (Rivera,2011; Park et al.,2013; Schemenauer & Joe,1989), but there has not been any documented attempt to measure it. In fact, previous studies used the shade coefficient beacuase this parameter is provided by manufacturers of mesh. However the shade coefficient describes the ability of a mesh to absorb or reflect solar radiation so it depends on the transparency of the material, mesh size and texture of the mesh, while fog harvesting does not depend on the transparency factor of the material. The shade coefficient is measured by manufacturers using a luxmeter. Samples of 50x50 cm. mesh, are put in a black box at a distance of 98 cm. from the lighting source (a 50 W incandescent lamp powered with stabilized voltage) and at a distance of 2 cm from the luxmeter cell. The shade coefficient is then defined as the ratio between luxmeter measurements with and without the net sample (Castellano et al.,2008).

All previous literature on fog collection uses the shade coefficient to characterize the collection mesh (Park et al.,2013;Rivera,2011;Schemenauer & Joe,1989), but we propose to use solidity instead, since the material transparency does not affect collection efficiency.

Solidity is an important parameter of a mesh to characterize it in terms of its resistance to airflow. Many authors measured solidity of insect-screens (Valera et al.,2006; Bailey et al.,2003; Miguel et al.,1997; Teitel et al.,2009) to relate it to the pressure loss caused by the screens, and then calculated the negative effect on greenhouse ventilation. There is no consensus on how to measure the solidity of a mesh. Cohen and Fuchs (1999) evaluated solidity with three methods: radiation balance, interception of solar radiation, and analysis of images of materials. They chose radiation balance as the best method to measure solidity, which was effective because their experiments considered only opaque mesh materials. However, most plastic meshes are not made of opaque material but rather semi-transparent fibers that allow radiation transmission. Teitel et al. (2009) and Valera et al. (2006)) estimated porosity as a function of woven density and pore size, which is effective for regular mesh, but does not consider local deformations that modify its porosity. Miguel et al. (1997) and Bailey et al. (2003) did not comment on the development of a method to measure solidity.

Two dimensional solidity (ς) is the relationship between the surface area of the fibers projected on the mesh plane (A) and the total area of the mesh plane (A_t).

$$\varsigma = \frac{A}{A_t}, \tag{2.1}$$

On the other hand, porosity (α) is the complement of solidity since it represents the area of open spaces in the mesh (A_{op}) divided by the total area of the screen (A_t).

$$\alpha = \frac{A_{op}}{A_t}, \tag{2.2}$$

$$\varsigma = 1 - \alpha. \tag{2.3}$$

For a regular square mesh, with constant fiber diameter and no knots at the thread intersections, solidity can be easily calculated using two mesh parameters: the fiber diameter (2R) and the void space between two fibers (2D) (Figure 2.1). Thus, solidity can be calculated as:

$$\varsigma = 1 - (\frac{1}{1 + D^*})^2, \tag{2.4}$$

with $D^* = \frac{R}{D}$.

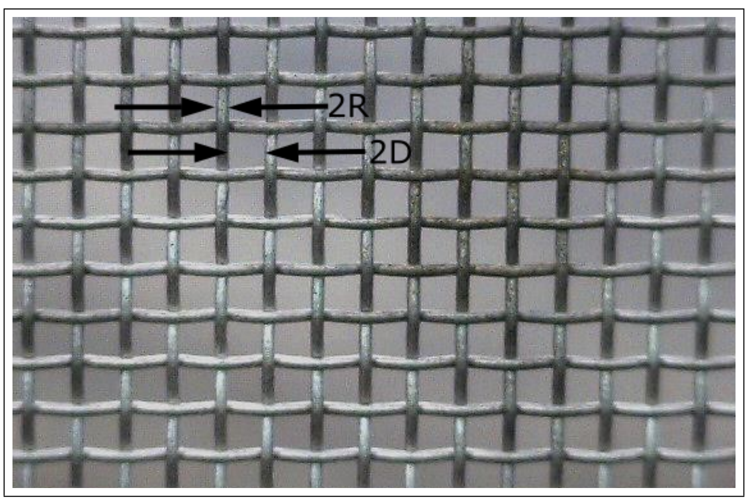

FIGURE 2.1. Simple woven metal mesh. The radius, R, of the fibers and half-spacing, D, between fibers are well defined. Solidity of such a mesh is given by the equation 2.4

Teitel et al. (2009) proposed that for a woven mesh that is made of a mono-filament thread and that has a simple texture, solidity can be calculated from the geometric dimensions of the screen:

$$\varsigma = 1 - \frac{D_x D_y}{(D_x + R)(D_y + R)}, \tag{2.5}$$

where D_x and D_y are the half spaces between two adjacent weft and warp threads, respectively. This solidity becomes equation 2.4 for a square mesh.

Valera et al. (2006) defined the average length of the pores in the two main directions of the mesh:

$$2D_x = \frac{1}{\rho_y} - 2R; 2D_y = \frac{1}{\rho_x} - 2R, \tag{2.6}$$

where ρ_x and ρ_y represent the number of fibers per unit of length (fibers m^{-1}) in each of the two main directions.

Equations 2.4 and 2.5 are simple ways to characterize the solidity of a regular mesh, but they do not consider that thread width can be irregular, and the presence of knots in most plastic meshes are not accounted for. Also, many meshes are subjected to treatments that deform and locally modify the geometric structure of the mesh, thus modifying its solidity. However the greatest need to improve the measurement method of solidity arises from the challenge posed by irregular meshes such as Raschel mesh. Raschel mesh is a knitted filament mesh and it has been widely used in agriculture as a shading net for crops and as a windbreak. Most fog harvesting systems also use Raschel mesh to collect the droplets of water. Figure 2.2 shows two samples of Raschel mesh. It can be seen that the samples has different projected fibers width and therefore different solidity.

In fog harvesting, it is common to use a double layer Raschel mesh, where the solidity may be quite different depending on the alignment of the layers and amount of stretching (due to wind, for example), . This variability is apparent in figure 2.2 (C), where the mesh covers a greater area at the top than at the bottom. Taking all this into consideration, it is clear that calculating the solidity of various types of mesh, especially double-layer Raschel mesh, is a difficult task.

We propose computer-aided image processing as a way to easily and reliably measure the solidity of any mesh. The objective is to develop a functional process by which a high-contrast close-up photograph can be taken of any mesh and be analyzed for its solidity using computing software (ImageJ, available from the NIH for free download at http://rsbweb.nih.gov/ij/). This aproach has been done before by Kenney (1987) and more

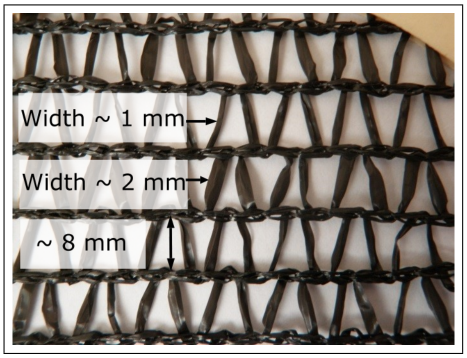

(A) Sample n1 of Raschel mesh.

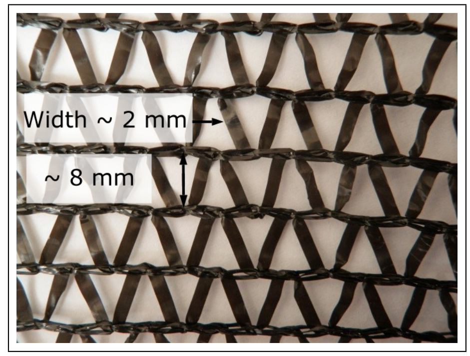

(B) Sample n2 of Raschel mesh.

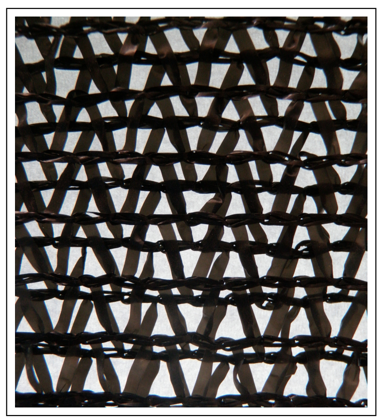

(C) Double layer of Raschel mesh.

FIGURE 2.2. Comparison of two Raschel 35% SC meshes and double layer Raschel mesh.

recently by Álvarez, Oliva, and Valera (2012), who developed a software to measure geometric properties of anti-insect meshes.The software was not focused on solidity alone, but included other parameters such as the density of fibers in each direction and the fiber diameter. The software assumes that each open space in the mesh is bordered on four sides by four fibers and thus can be represented by a quadrilateral, but this is not accurate for simple or double layer Raschel mesh. Although the solidity of irregular meshes can still be measured with the software developed by Álvarez et al. (2012), we propose an alternative and more accessible method that provides accurate results using a basic digital camera and an open source software.

2.2. Material and Methods

The meshes tested have a pore size on the order of a few milimeters. They are of irregular shape and one of three types of material: opaque, reflective or semi transparent. Most meshes tested are shown in figure 2.3. The method to measure two dimensional solidity consists of taking a photo of the mesh and converting it into a binary black and white image based on a certain threshold value. Then ImageJ reports the number of pixels representing the mesh as well as the total number of pixels in this image. The solidity is a value between zero and unity obtained when the number of mesh pixels is divided by the total.

2.2.1. Method for photographing meshes

The first step in obtaining solidity by the image analysis method, and the most important for obtaining usable results, is taking a photo representative of the mesh. Photos in this work were taken using digital cameras. Some argue that scanning technology yields high resolution images while avoiding the problem of lens distortion (Grove & Jerram,2011). However, one of our goals is accessibility, and someone interested in measuring solidity is more likely to have a digital camera than a scanner with the necessary capabilities. A camera also offers the flexibility of taking photos in the field of three-dimensional meshes.

In lab, the camera was mounted on a tripod for stability and faced the mesh squarely. The shutter-delay function further prevented camera shake from pressing the shutter button. Photographs were close-up, but with some variation in level of zoom. Smaller apertures produce better images and help prevent vignetting effect, which is a reduction of the image brightness at the periphery compared to the image center. Also slow shutter speeds were used. Photos were taken using two different lighting styles: backlit and frontlit. In both cases the objective was for the silhouette of fine meshes to show clearly and produce images with high contrast. Using the backlighting method, the mesh lay flat on a light table in

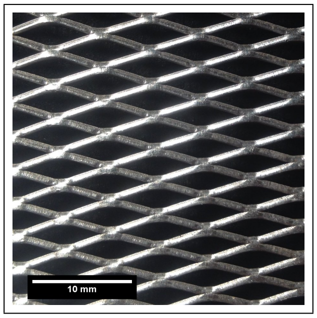

(A) Expanded aluminum.

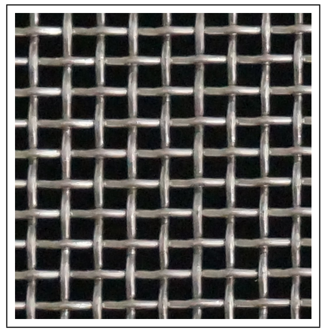

(B) Steel woven.

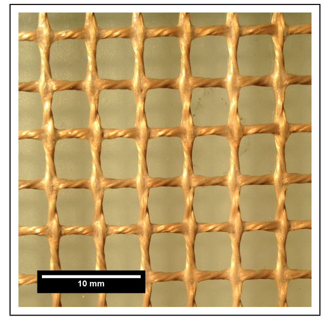

(C) Opaque woven.

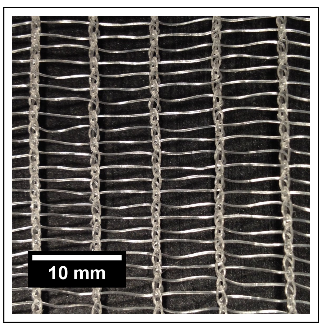

(D) Knitted round 1.

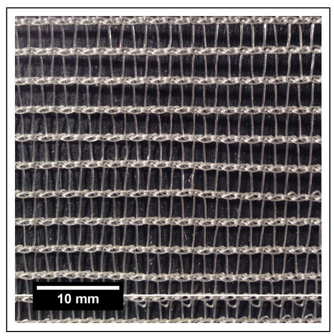

(E) Knitted round 2.

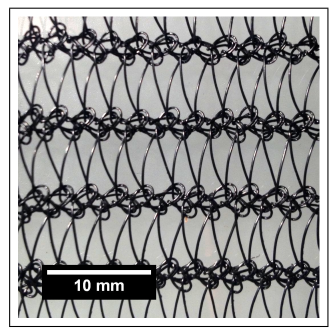

(F) Knitted round 3.

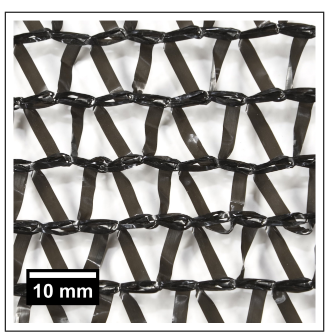

(G) Knitted ribbon 1.

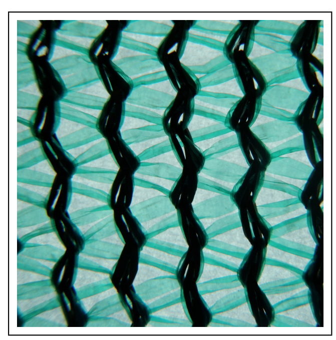

(H) Knitted ribbon 2.

FIGURE 2.3. Meshes measured

a dark room and photographs were taken from above. This was the preferred method for most meshes, and with adequate post-processing, provided acceptable images for all meshes tested. However, frontlighting better distinguished the edges of fibers for metallic, reflective meshes. For this, mesh samples were placed on a matte black background in a well-lit space.

2.2.2. Validation with control image

The accuracy of this method was tested with a series of control images with known solidity (0.5 and 0.75). First, perfect computer-generated images were analyzed as shown in Figure 2.4, and returned exactly the values of solidity expected. This confirmed that the software functions correctly. Error due to the camera was investigated to ensure that the solidity of a mesh would not be altered when processed as an image. Photographs taken of print-out images were analyzed. Although printer error could not be separated from camera error, the overall error was found to be between 1 and 3 percentual points, as defined by the following equation:

$$E = |\varsigma_{obs} - \varsigma_{act}| \cdot 100 \tag{2.7}$$

where ς_{obs} is the measured solidity and ς_{act} is the real solidity.

We printed 3 sets of 3 meshes each. Each set contained a 0.25, 0.50 and a 0.75 solidity mesh. The difference between each set was the fiber width (2R). Set 1 had 1 mm fibers; set 2, 2 mm fibers; and set 3, 3 mm fibers. Figure 2.5 illustrates the results, showing an increase in error as the fiber width decreased. This occurs because it is difficult to accurately discern the edge of the fibers and the smaller the fiber width, the more difficult is to discern it. This is illustrated in figure 2.6, where figure 2.6(a) shows the detail of a printed 0.5 solidity mesh, with 1 mm thread width, while figure 2.6 (b) shows the detail of printed 0.5 solidity mesh, with 3 mm thread width. The latter has better results because of its greater fiber width. The same result was observed in real meshes, where the accuracy of the solidity measurement can be affected by the 2R parameter. In order to decrease the error associated with fiber width it is advisable to take the picture closer to the mesh. Nevertheless, if the mesh is arbitrary framed (the correct way to position the mesh is to have the borders of the image located midway between adjacent fibers) and if the image has less than five pores, then solidity measured may have an error of more than 10 percentage points for solidities lower than 0.2. Thus, photographs have to be taken as close as possible to the mesh, but keeping in mind that the closer the image (and thus the less the number of pores in the image) the more important is to frame the mesh correctly.

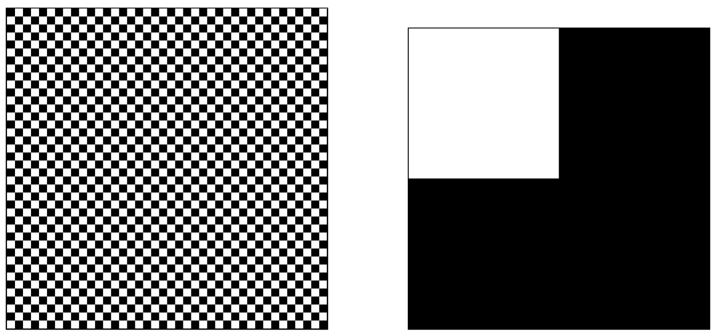

(A) Control Image ς=0.5

(B) Control Image ς=0.75

FIGURE 2.4. Control images were used to test solidity measurements.

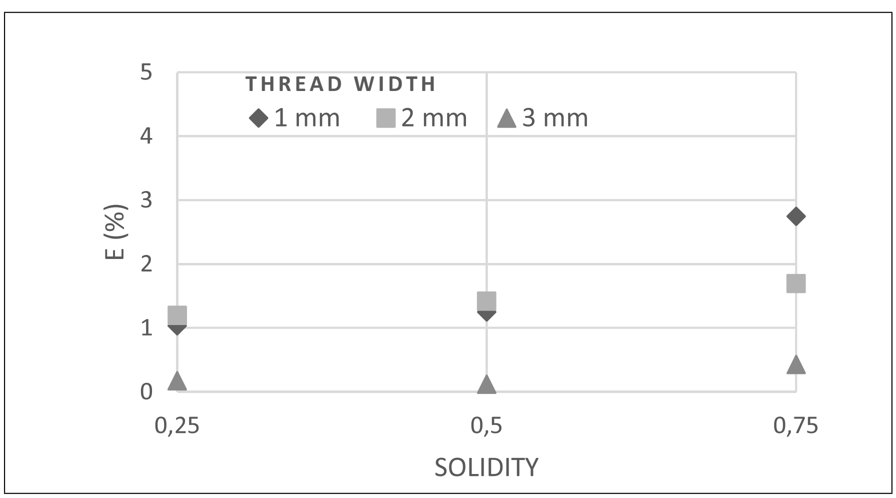

FIGURE 2.5. Error measured in the calculation of solidity of control printed meshes using equation 2.7

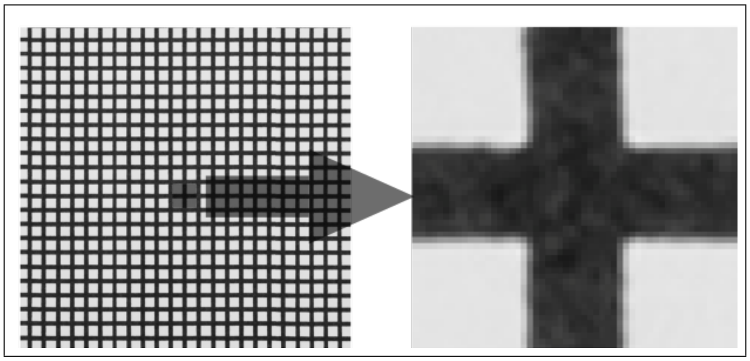

(A) Printed mesh 1 mm thread width and controled $\phi = 0.5$

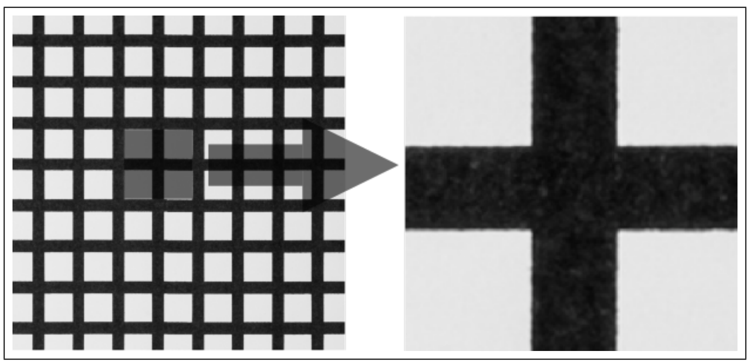

(B) Printed mesh 3 mm thread width and controled $\phi = 0.5$

FIGURE 2.6. Printed Meshes. The thread width is an important parameter since it is harder to distinguish the edge of the fibers with small width, affecting the solidity measure.

2.2.3. Adjusting quality of image conversion through the threshold parameter

The most challenging step in calculating an accurate solidity is the conversion of the original, greyscale image into a binary black and white one. Computer images are defined by matrices, where each component of a grayscale image matrix represents a pixel. When converting to binary, all pixels below a specified intensity level become black (value of 0), and all pixels above become white (value of 255). The ImageJ Auto threshold function contains several programmed algorithms to automatically choose a threshold level between light and dark pixels.

When there is not enough contrast between the mesh and the background, as in images of light-colored, non-opaque meshes, or when the mesh fibers have differing intensities, as in images of multilayered or multicolor meshes, the Default setting is not adequate. This is clearly observable in the resulting binary image, such as seen in figure 2.7. In this case, a more appropriate level is chosen by an alternate algorithm, which can be determined by the try all method.

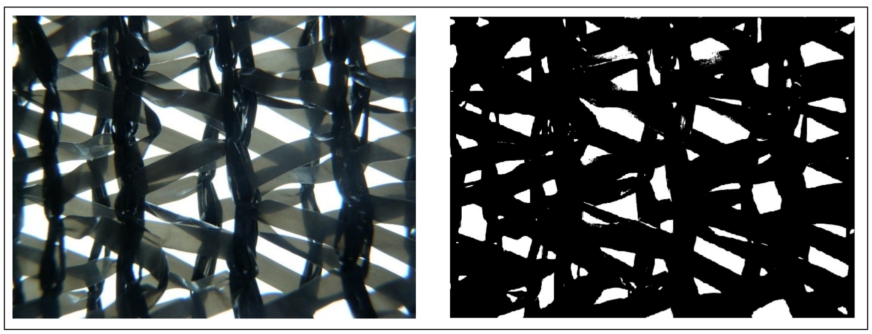

(A) On the left, the fibers in a triple layer of Raschel mesh appear to have varyng shades. On the right, ImageJ automatically sets a threshold level of 141, which seems to be an acceptable result.

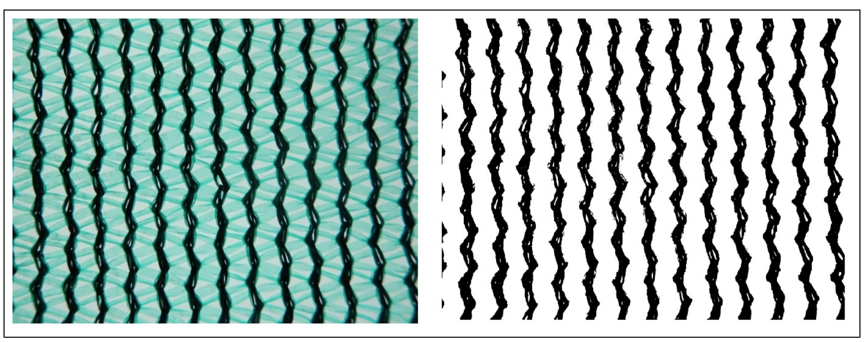

(B) On the left, the light green fibers in this Raschel mesh contrast poorly against the white background. On the right, ImageJ automatically sets a level of 104 which completely omits the light green fibers

FIGURE 2.7. Examples where graytresh fails to set an appropiate level.

A sensitivity analysis was conducted in ImageJ to investigate the effect of chosen threshold on solidity calculated. The tool plotted a histogram with the gray distribution of the image. Ideally the distribution has two peaks with zero or near-zero frequency of

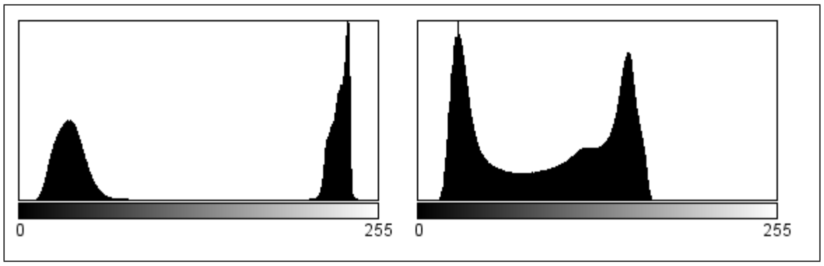

FIGURE 2.8. On the left, an example of a mesh with high contrast against the background. In this case, solidity can be easily computed as the number of pixels on the left peak, divided by the total amount of pixels in the image. Notice that the threshold value can be set in a large range without affecting solidity very much. On the right, a histogram of a mesh that contrast poorly against the background.

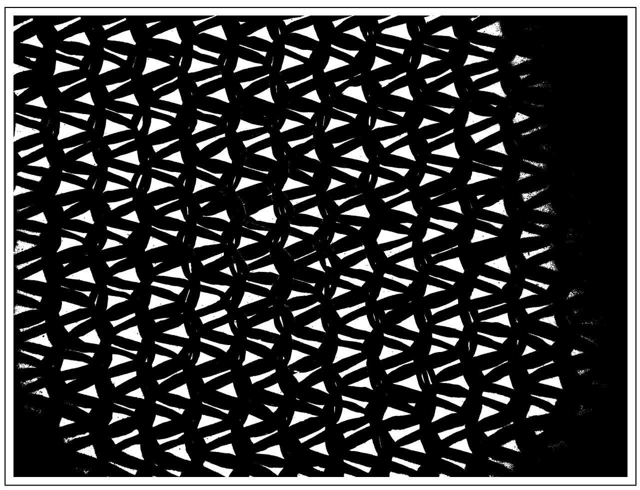

FIGURE 2.9. Green Raschel mesh at best level setting of 198 which gives a solidity of 0.88. This image cannot be analyzed for solidity in current state.

pixels in between, as shown in figure 2.8 (left), so that variation in the choice of level has a negligible effect on the calculation. If this is not the case, as shown in the examples in Figure 2.8 (right), it becomes much harder to obtain a trustworthy value.

Sometimes a level appropriate for converting the whole image does not exist, and some portions of mesh are always omitted, while some spaces are included. This occurs with very light or translucent mesh and multicolor mesh, such as the green Raschel mesh of Figure 2.7 (b). The level with the best results still produced an unusable image, shown in figure 2.9.

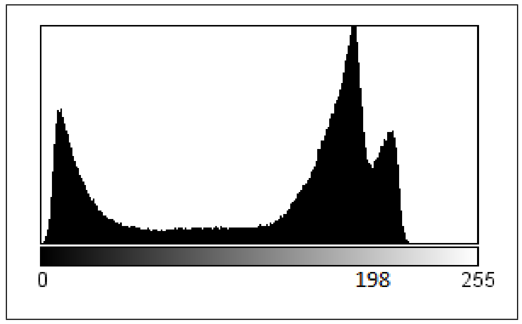

FIGURE 2.10. Histogram of green Raschel mesh. The threshold value was manually set in 198.

Several possible solutions were investigated. These included adjustments in image capture and in image processing. Image capture fixes included decreasing camera exposure, taking a picture from a smaller distance, extracting a useful portion of the image, and darkening the mesh with either carbon black or spray paint before taking pictures. Of these, extraction of a part of the image and spray painting proved most successful. However, the most effective and simplest fix was in the image processing step, because in this we can identify in the histogram peaks corresponding to predominant grey value in the image. In other words, meshes with two different colors may have a histogram with three peaks (one is the background and the other two are the predominant greys of the grey scale image of the mesh). Figure 2.10 shows the histogram of the green Raschel mesh, where, if we manually choose a threshold value in between the two peaks (198 in this case) and then extract the centre of the image, the result becomes an acceptable binary image, as is shown in figure 2.11 which has a solidity of 0.84.

Another issue arises for meshes with round fibers, like the woven steel mesh. Light reflects differently from different parts of the fibers, thus creating a visible gradient in the image. While this effect allows the eye to perceive depth, it is detrimental to measuring solidity because the image conversion is sensitive to the choice of threshold level. If not correct, the outer edges of the fibers are omitted, or part of the background is included. In addition, the smooth transition from fiber to background makes the correct cutoff level difficult to identify by eye. The solution is to modify the image capture step from backlit to the frontlit method.

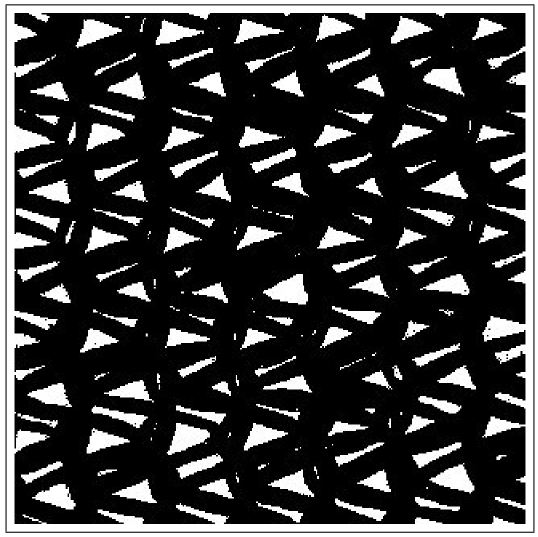

FIGURE 2.11. Binary image of the centre of the original image of the green Raschel mesh. In this case, solidity becomes 0.84.

2.2.4. Accounting for variability

The more irregular a mesh is, the more variable the solidity determined for images of different sections. To gain better understanding of a mesh, it is useful to divide images into subsections and compute local solidities across each image. With this approach, each photograph must include a significant area of mesh without losing detail. If the mesh has both a large area and high variability, like in a double layer Raschel fog-collector, gathering information from several pictures taken from disparate points across the mesh produces a more accurate result.

2.3. Results and Discussion

The binary images of the meshes tested are illustrated in figure 2.12 and the results are summarized in table 2.1.

2.3.1. Comparison of the Raschel mesh nominal shade coefficient against the solidity parameter

Raschel meshes are sold at various nominal shade coefficients (SC). We studied the 35% SC Raschel mesh (labeled as knitted ribbon 1). The goal was to compare the given SC

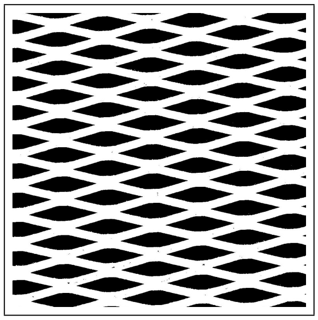

(A) Expanded aluminum.

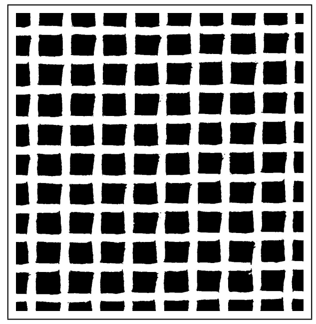

(B) Steel woven mesh.

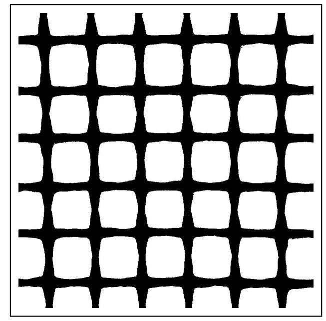

(C) Opaque woven.

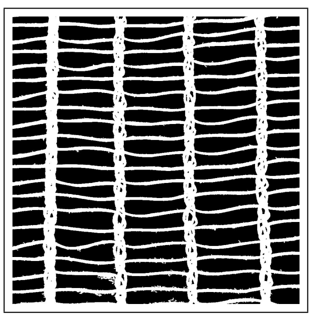

(D) Knitted round 1

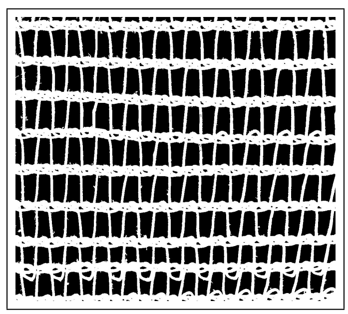

(E) Knitted round 2

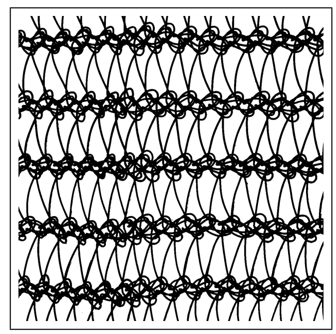

(F) Knitted round 3

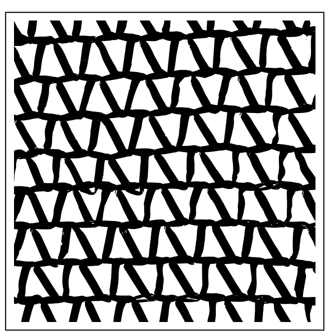

(G) Knitted ribbon 1

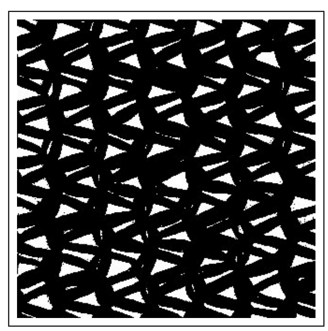

(H) Knitted ribbon 2

FIGURE 2.12. Binary image of the meshes tested

TABLE 2.1. Solidity measured

Mesh	Solidity
Expanded aluminum	0.55
Steel woven	0.47
Opaque woven	0.35
Knitted round 1	0.34
Knitted round 2	0.39
Knitted round 3	0.37
Knitted ribbon l	0.47
Knitted ribbon 2	0.84

(used as solidity by previous fog harvesting studies) against the solidity measured by our method. Photographs taken of these samples yielded that the solidity of Raschel 35%SC was 0.47. Taking the solidity calculated by image analysis as the true value, this indicates an error of 26% in the reported nominal solidities (actually reported as shade coefficient) in fog harvesting studies. Figure 2.13 illustrates the analysis of the 35% SC Raschel mesh.

On the other hand, using equation 2.5 and 2.6, solidity of Raschel mesh can be calculated as

$$\varsigma_{Raschel} = 1 - \frac{(H - 2R) \cdot (D - 2R)}{H \cdot D} \tag{2.8}$$

where H is the average distance between two transversal knitted threads (in m), 2R is the average thread width (m), and D is the average transversal distance of a longitudinal thread (m). Figure 2.14 shows the parameters used for a Raschel mesh. In the 35% SC Raschel mesh, we estimated H=0.008 m, 2R=0.002 m, and D=0.005 m. With those values, using equation 2.6, solidity is $\varsigma 35\% SC = 0.55$.

Equation 2.8 overestimates the solidity of Raschel mesh since it considers a constant thread width of 2 mm, when in fact 2 mm is the maximum projection of the thread. Notice that using a thread width of 1.68 mm, solidity calculated with equation 2.8 becomes the same 0.47 measured by our method, which serves to validate it, because projected thread width seems to be more likely 1.68 mm than 2 mm.

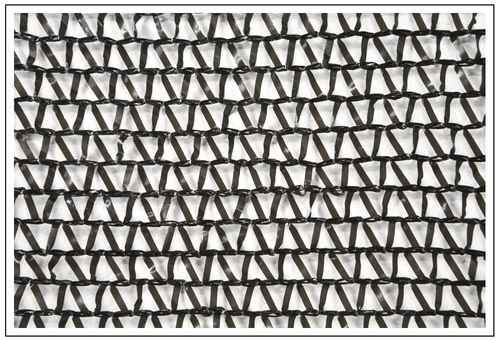

(A) Raw photograph.

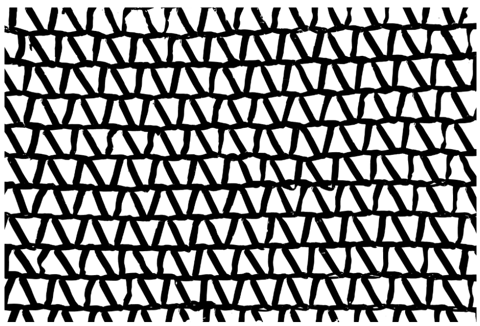

(B) Binary image of the raw photograph.

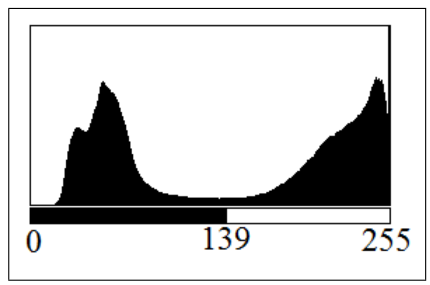

(C) Histogram of the white intensity of the pixels in the raw photograph (0 is black, 255 is white).

FIGURE 2.13. Analysis of 35% SC Raschel mesh.

2.3.2. The effect of multiple Raschel layers

The greatest unanswered question before developing the image analysis method was how to determine the solidity of a double layer of mesh. With this method, the solidity of multiple layers is measured as easily as a single one. There are two main differences. If a third or fourth layer is added, fibers in the image start to take on different shades, depending on how much they overlap with fibers of other layers. This may complicate the use of ImageJs auto threshold function, since it may set the threshold level too low, and omit the lightest fibers. In this case, the other option must be used for the threshold method, as discussed in section 2.2.3.

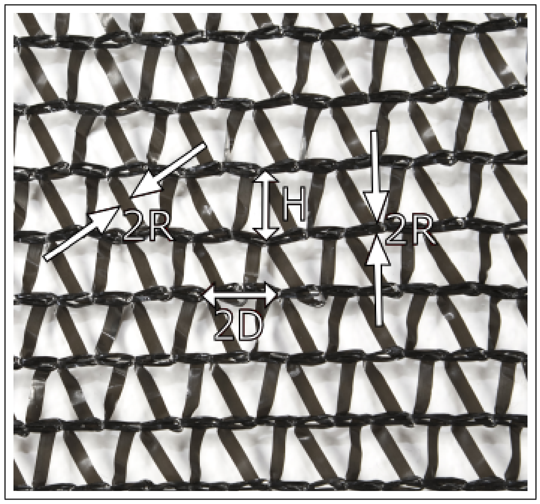

FIGURE 2.14. Parameters used to calculate solidity of a Raschel mesh using equation 2.6.

The second difference to keep in mind is that solidity will depend on how much the layers align when overlapped. Figure 2.15 shows two possible configurations, where a high level of alignment produces a lower solidity (0.65) than a low level of alignment (0.71). Therefore it is informational to report minimum and maximum values as well as an average. This variability is most prominent for double layers, because as more layers are added a large fraction of available area is covered regardless of configuration, and the probability of perfect alignment is low.

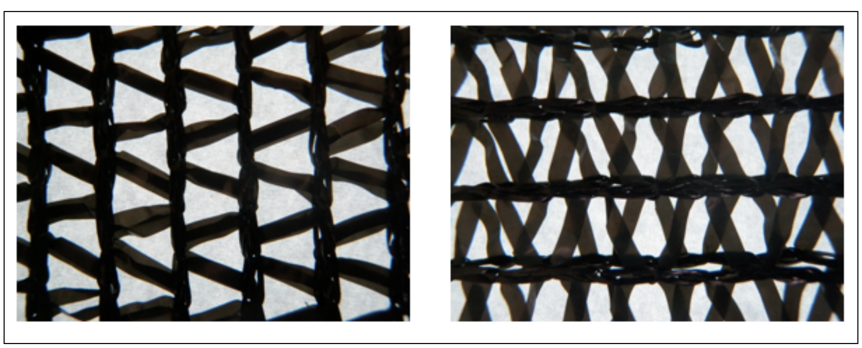

FIGURE 2.15. Possible levels of mesh alignment in a double-layer. On the left, layers are nearly perfectly superimposed, appearing like a single layer with thick fibers, resulting in a 0.65 solidity. On the right, layers are offset, with a 0.71 solidity

Although more than two layers of Raschel mesh have not been used in fog-collectors or agriculture, it is instructive to study the effect of additional layers. For a number of layers ranging from one to four, we measured the solidity of ten images for each case. These are plotted in figure 2.16. Intuitively, solidity does not increase linearly, the curve is concave down. With more layers, we reasonably expect solidity to rise asymptotically to a value of one.

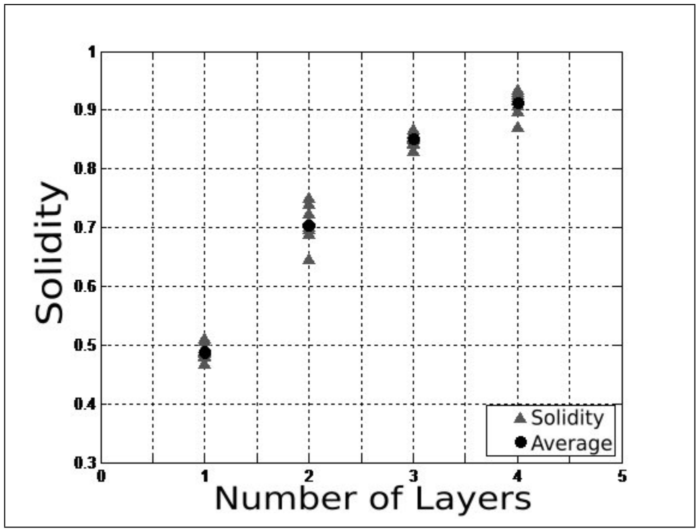

FIGURE 2.16. Effect of multiple Raschel Layers on 2d solidity

3. AERODYNAMIC ANALYSIS OF FOG COLLECTING MESHES

3.1. Introduction

Fog represents a large source of fresh water for arid and foggy regions. Fog collection technology appears to be an extremely promising and low-cost water harvesting system for human consumption, industrial and irrigation purposes (Schemenauer & Cereceda,1992; Klemm et al.,2012; Park et al.,2013). Fog water can be collected in large quantities by fog collectors, structures composed of a large mesh held by poles or a frame, perpendicular to the wind driven fog. Over time, many different designs have been used, but presently the screen type collector is the most common for the production of significant amounts of water (Abdul-Wahab & Lea,2008).

Fog harvesting yields, usually expressed as liters per square meter of mesh per day ($l/m^2/day$), annual average, depend on the liquid water flux of the fog reaching the collector and the collection efficiency of the mesh. For a given site and orientation of the collector, ie. a given liquid water flux, the main factor that affects this yield is the mesh collection efficiency. As Rivera (2011) argued, the cost of the mesh represents a small percentage of the total cost of the installation, typically less than 10% of the materials alone and probably less than 5% considering labor and transportation. Therefore, even a large increase in cost for a more efficient mesh will cause a relatively small increase in the total cost of the fog collector, resulting in a lower cost of the collected water.

Usually fog collection projects have not been of commercial interest because of its cost compared to the amount of water collected. Indeed LeBoeuf and Jara (2014) conclude that fog collection projects could be profitable given an average collection rate of over 10 $l/m^2/day$. However, the typical yields of fog collection projects are 3 to 5 $l/m^2/day$, reaching up to 8 $l/m^2/day$ in very few places, like Alto Patache in the Tarapacá region, Chile (Cereceda et al.,2002). To get yields of 10 $l/m^2/day$ or more it is necessary to improve collection efficiency of fog collectors.

The fundamentals of collection efficiency has been studied by a small number of authors. Rivera (2011) proposed that the overall collection efficiency (η_{coll}) can be determined by the product of three efficiencies:

$$\eta_{coll} = \eta_{AC}\eta_d\eta_{dr} \tag{3.1}$$

where η_{AC} is the aerodynamic collection efficiency, η_d is the deposition efficiency, and η_{dr} is the draining efficiency. The latter refers to the fraction of the water captured by the mesh that actually reaches the gutter, some of the captured water is lost by re-entrainment and spill. Re-entrainment losses have been studied by Park et al. (2013), however in the present study the draining efficiency (η_{dr}) will be considered equal to 1. Deposition efficiency (η_d) in turn quantifies the fraction of fog droplets that are actually deposited from the population initially headed toward the solid filaments of the mesh. Park et al. (2013) proposed that solid structures placed in a wind stream (with unperturbed velocity u_0) deflect the air, but the fog droplets (with radius r_{fog}) have a tendency to migrate across streamlines, because of their higher inertia, and impact the filaments. This migration is controlled by the Stokes number (St), which captures the ratio of the response time of a particle to that of the surrounding flow:

$$\eta_d = \frac{St}{St + \pi/2} \tag{3.2}$$

$$St = 2\rho_{water}/9\rho_{air} \cdot Re_R(r_{fog}/R)^2 \tag{3.3}$$

where ρ_{water} and ρ_{air} are the densities of the droplet and air, respectively, R is the half width of the filaments (for round filament meshes, R is equivalent to the radius of the thread) and $Re_R = \rho_{air}u_1R/\mu_{air}$ is the Reynolds number, where μ_{air} is the viscosity of air and u_1 is the wind velocity reaching the mesh.

Aerodynamic collection efficiency (η_{AC}) has been studied by Rivera (2011) who defines it as the portion of droplets in the unperturbed fog that would collide with the mesh. Thus, the fraction of the upwind undisturbed flow that passes through the mesh depends on the balance between the large scale drag on the mesh and the pressure drop of the airflow through the mesh. The aerodynamic collection efficiency defined previously is

$$\eta_{AC} = \frac{\varsigma}{1 + \sqrt{\frac{C_0}{C_d}}} \tag{3.4}$$

where ς is the two dimensional solidity (or solidity) of the mesh, defined as the ratio between the projected surface area of the threads and that of the total mesh. This parameter has been called as shade coefficient in many papers of fog collection (Rivera,2011, Schemenauer & Joe,1989, Park et al.,2013, Domen, Stringfellow, Kay, & Gulati,2014), but essentially shade coefficient describes the ability of a net to absorb or reflect a certain part of solar radiation, so it also depends on the transparency of the material, while fog harvesting does not depend on this factor. For this reason we preferred to call it solidity, which is the complement of porosity, used in fog collector studies by Bresci (2002) or in anti-insect screens studies (Valera et al.,2006; Bailey et al.,2003; Miguel et al.,1997; Teitel et al.,2009; Álvarez,2010; Muñoz, Montero, Antón, & Giufrida,1999); C_d is the drag coefficient of a non-permeable screen and, therefore, is independent of the solidity; and C_0 is the pressure loss coefficient and it depends on solidity and the structure of the mesh.

Finally, with the draining efficiency considered as 1, the overall collection efficiency will be

$$\eta_{coll} = \eta_{AC}\eta_d \tag{3.5}$$

This study focuses on improving η_{AC} by looking for meshes that have lower pressure drop for the same solidity.

3.2. Theoretical Basis

The traditional approach to macroscopically characterize the airflow through a porous media is to use the Forchheimer equation (Miguel et al.,1997;Valera et al.,2006;Teitel et al.,2009):

$$-\frac{\partial P}{\partial x} = \frac{\mu}{K_p}u + \rho(\frac{Y}{K_p^{1/2}})u^2 \tag{3.6}$$

where P is the pressure in Pa; x the first horizontal Cartesian coordinate in m; μ the dynamic viscosity of the fluid in $kg \cdot s^{-1} \cdot m^{-1}$; K_p the permeability of the porous medium in m^2; u the speed of fluid at the pores of the mesh in $m \cdot s^{-1}$; ρ the air density in $kg \cdot m^{-3}$; and Y the non-linear momentum loss coefficient or inertial factor. Equation 3.6 is not a purely empirical expression, since it can be derived from the Navier-Stokes equation for one-dimensional, steady incompressible flow of a Newtonian fluid in a rigid porous medium (Molina, Valera, A.J., & Madueno,2006).

Forcheimmer equation can be used to describe the airflow through a mesh, but this requires values for the permeability K_p, the inertial factor Y, and the thickness ∂x of the screen. The parameters K_p and Y can be obtained from measurements of pressure differences across the screen and the resulting airflow, by fitting the pressure difference as a quadratic function of air speed and, then, comparing the coefficients with those of equation 3.6. However, for many screens the thickness is ill defined and, although equation 3.6 represents the flow resistance characteristics of a porous material, its practical application is not straightforward (Bailey et al.,2003).

For a steady, non-viscous flow, the Navier-Stokes equation can be integrated along a streamline to obtain the Bernoilli equation. Instead of permeability some authors (Bailey et al.,2003; Guan, Zhang, & Zhu,2003; Molina et al.,2006) use the pressure loss coefficient, resorting to Bernoilli's equation, to characterize a screen (Miguel et al.,1997). Thus, pressure loss across the screen (ΔP) can be expressed as:

$$\Delta P = \frac{1}{2} C_0 \rho_{air} u^2 \tag{3.7}$$

where C_0 is the pressure loss coefficient, ρ_{air} is the air density and u is the upstream wind speed. The pressure loss coefficient C_0 is a function of solidity, Reynolds number and filament characteristics. In a high-Re turbulent flow the pressure loss coefficient is largely independent of Re and is a function of solidity and filament characteristics. At low Re the flow becomes laminar and the pressure loss coefficient increases as Re decreases (Teitel et al.,2009).

In porous media there are several ways to define the Reynolds number, depending on the characteristic dimension. Some authors use the square root of permeability as the characteristic dimension (Re_k), while others use the thread diameter (Re_R). Nevertheless, in highly porous medium, which is the case of the meshes tested in this study, the best method to characterize the flow is to use the pore characteristic size (Antohe & Lage,1997,Boomsma & Poulikakos,2002). Thus, Reynolds number based on the pore diameter (D_p) is

$$Re_p = \frac{\rho u D_p}{\mu} \tag{3.8}$$

Miguel et al. (1997) conclude that the pressure loss coefficient will be appropriate only when advective inertia effects are dominant. At $Re_p > 150$, the viscous forces do not dominate the flow, and therefore the first term of the right side of equation 3.6 can be discarded, obtaining equation 3.7.

In any case, Muñoz et al. (1999) applied equation 3.6 and 3.7 to the case of an anti-insect screen with a pore size of 0.11 mm, and showed that the two equations give very similar results for a range of air speeds between 0 and 3 $m \cdot s^{-1}$. As the pore size of the screen was increased, the difference between the values calculated by the two equations decreased. (Miguel et al.,1997;Bailey et al.,2003).

Pressure loss coefficients (C_0), and permeability (K) for different nets have been widely studied (Valera et al.,2006; Bailey et al.,2003; Miguel et al.,1997;Teitel et al.,2009; Álvarez,2010; Muñoz et al.,1999; Idel'cik,1960). Nevertheless, those parameters have been determined for only some types of meshes, which include anti-insect screens, thermal screens, silk and wire meshes, but typical meshes used in fog collectors, such as Raschel mesh (made of knitted filaments of polyethylene) have not been characterized yet . This work aims at characterizing in terms of C_0 three kind of meshes: knitted ribbon filaments, knitted round filaments and woven round filaments,in order to shed light on how to increase aerodynamic collection efficiency.

3.3. Material and Methods

3.3.1. Wind tunnel system

A low-speed, open-circuit wind tunnel of the suction type with square cross-section was designed and built at the Department of Mechanical Engineering of Pontificia Universidad Católica de Chile. The wind tunnel length is 2.4 m with a square section of 0.4 x 0.4 m. Airflow enters through a converging section with a contraction area-ratio of 1:5 and a ratio between the entrance equivalent diameter and the length of the contraction of 0.88. Between the entrance and the test sections there is a flow straightener. To mount the sample, the tunnel can be divided in two parts with the test section in the middle. Figure 3.1 shows the wind tunnel.

Airflow is supplied by a centrifugal fan with backward blades (CLT-15 Soler & Palau, Santiago, Chile) with a capacity of 7000 m^3h^{-1} and impeller diameter of 401 mm, driven by a 1.1 kW induction, three-phase electric motor (230 V and 50 Hz). A variable frequency drive (ACS150 ABB, Santiago, Chile) was used for speed control, with an output frequency of 0-50 Hz and a set point resolution of 0.1 Hz. This allows the fan speed to vary from 0 to 1628 min^{-1}.

To characterize the flow in the wind tunnel it is necessary to evaluate Reynolds number based on the equivalent diameter of the test section. At the maximum speed of 8 ms^{-1}, the Reynolds number is over 10^5 and at 0.5 ms^{-1}, $Re > 4 \cdot 10^3$, which indicates the presence of turbulent flow over the full range of air speeds of interest.

3.3.2. Procedure and instrumentation

Once the mesh sample is placed in the test section, the variable frequency drive (VFD) is set to a specific frequency and, when stable airflow had been established, data collection began. Between 500 and 700 readings of pressure drop and velocity were taken in a 5 minutes interval. Then, the air speed is increased and data is collected again. The procedure continues until maximum frequency is reached (50 Hz). The a maximum pressure drop is limited to 50 Pa by the fan characteristics.

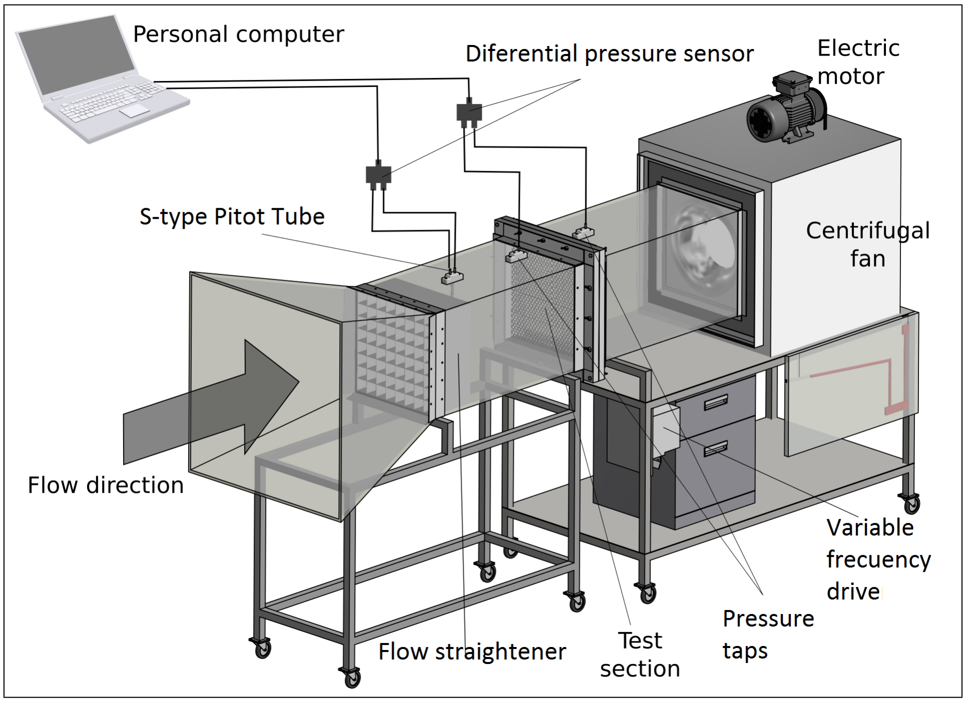

FIGURE 3.1. Wind tunnel used to measure the pressure difference and the air speed.

The static pressure drop through the test section was measured by a differential pressure sensor (model D6F-PH0505AD3, OMRON, US) connected to two 6 mm diameter tubes to probe static pressure at the center of the section, 150 mm upstream and 150 mm downstream the mesh. The readings were stored in a personal computer. The sensor measurement range was -50,+50 Pa and it was calibrated using an inclined water column manometer (Dwyer, Santiago, Chile).

A type S Pitot tube, placed 900 mm upstream from the sample, measured the air speed. Air speed can be deduced from the Bernoulli's equation applied in a streamline:

$$v = \sqrt{\frac{2P_d}{\rho}} \tag{3.9}$$

where P_d is the dynamic pressure, measured by a differential pressure sensor (D6F-PH0025AD1, OMRON, US) with a range of 0-250 Pa. Since it is necessary to calibrate both the type-S Pitot tube and the pressure sensor, the calibration was performed simultaneously using a hot wire anemometer (Testo, Germany). Air density was calculated from the air temperature measured with a thermometer incorporated in the differential pressure sensors.

3.4. Results and Discussion

Fifteen meshes were tested, measuring the pressure drop and the air speed for each one. Meshes were divided into three types: knitted ribbon filament (Figure 3.2), knitted round filament (Figure 3.3), and woven round filament (Figure 3.4). All knitted type meshes correspond to Raschel knitting. Results for knitted ribbon type meshes are shown in Figure 3.5 and for round filament, knitted and woven, in Figure 3.6. The woven round filament mesh was grouped with the knitted round filament meshes because whether the filament is round or a ribbon makes a bigger difference in pressure drop than whether the mesh is knitted or woven. The best fit equation for the pressure drop as a function of the air speed is a second order polynomial of the type

$$\Delta P = au^2 + bu \tag{3.10}$$

Equating the constants of the experimental polynomial (equation 3.10) to the ones of Forchheimer's equation (equation 3.6), allows to obtain expressions for the permeability K and the inertial factor Y. However, according to (Miguel et al.,1997) at $Re_p > 150$ viscous forces are not important and pressure loss can be calculated using the pressure loss coefficient as described in equation 3.7. For the meshes measured, Re_p is greater than 150 for air speeds over 1 ms^{-1}, except for the woven mesh that exceeds the viscous limit at 4 ms^{-1} due to its smaller pores. For simplicity, and to be consistent with equation 3.4 for the aerodynamic collection efficiency, we will apply equation 3.7 to all meshes, which implies to fit a polynomial of the type

$$\Delta P = au^2 \tag{3.11}$$

Table 3.1 summarizes the results of the polynomial fit for all the meshes, where solidity was measured by means of digital image analysis using the software ImageJ and C_0 was calculated with the coefficient a of equation 3.11. Although the coefficient of determination

R^2 of the polynomial fit corresponding to equation 3.10 is better than the one corresponding to equation 3.11, the last is still considered acceptable because is always over 0.98.

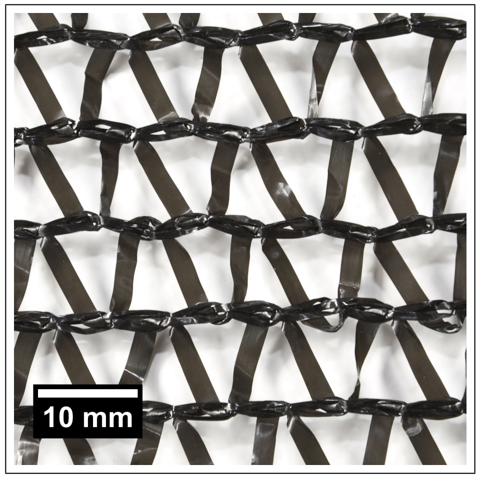

FIGURE 3.2. Knitted ribbon filament type mesh (K.RIBBON-5).

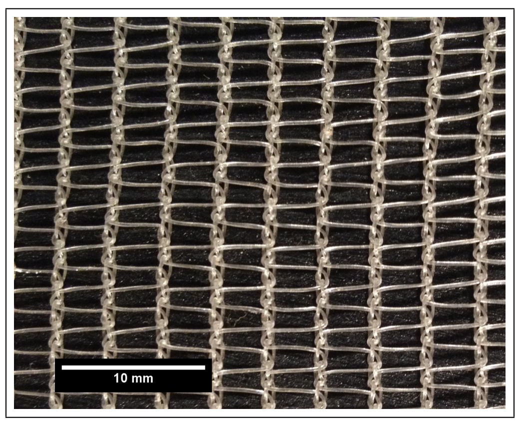

FIGURE 3.3. Knitted round filament type mesh (K.ROUND-2)

For the knitted ribbon meshes, the relationship between pressure loss coefficient and solidity is well represented by an exponential function as follows and shown in Figure 3.7,

$$C_0 = C_1 e^{C_2 \varsigma} \tag{3.12}$$

with $C_1 = 0.0744$ and $C_2 = 6.85$.

On the other hand, the five round filament type meshes measured have solidities ranging from 0.2 to 0.6. Due to lack of samples with higher solidity, we could observe only the

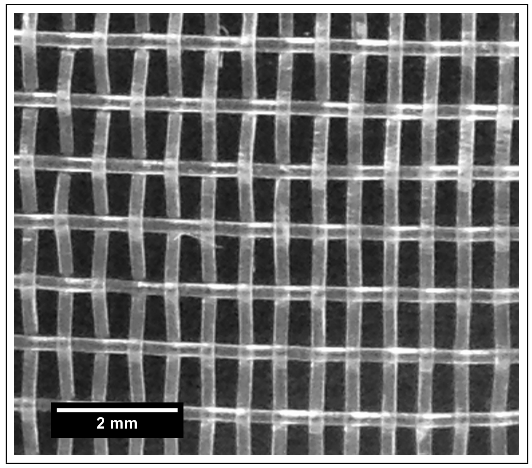

FIGURE 3.4. Woven round filament type mesh (W.ROUND-1).

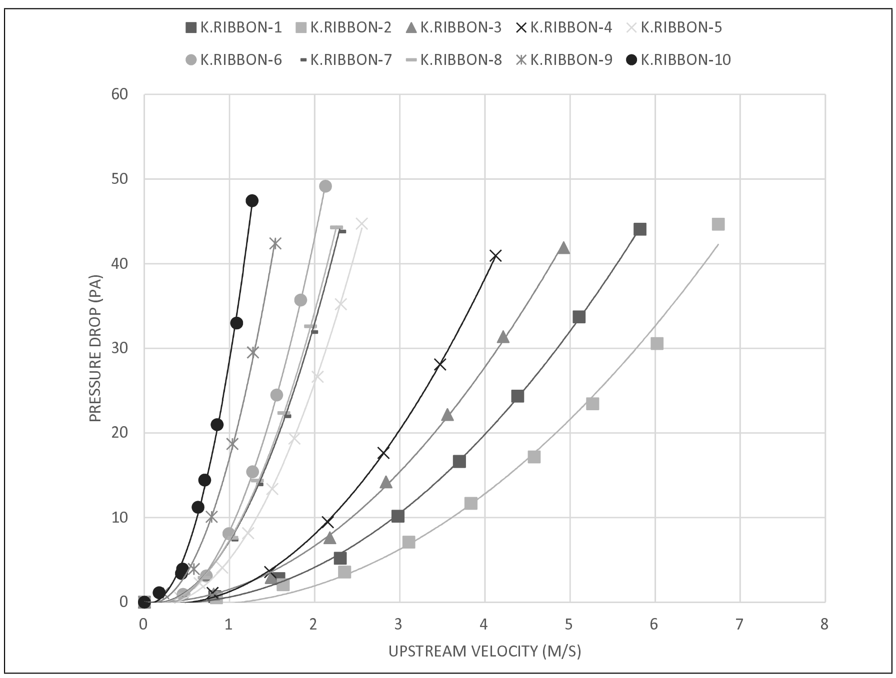

FIGURE 3.5. Pressure drop of the knitted ribbon filament meshes, fitted with equation 3.10

local behavior of the round filament curve, which best fit is a polynomial function. However, for higher solidity we expect the curve to behave as an exponential function, like the one found for ribbon meshes. For this reason, we opted to fit an exponential curve with $C_1 = 0.1192$ and $C_2 = 4.7526$, shown in Figure 3.8.

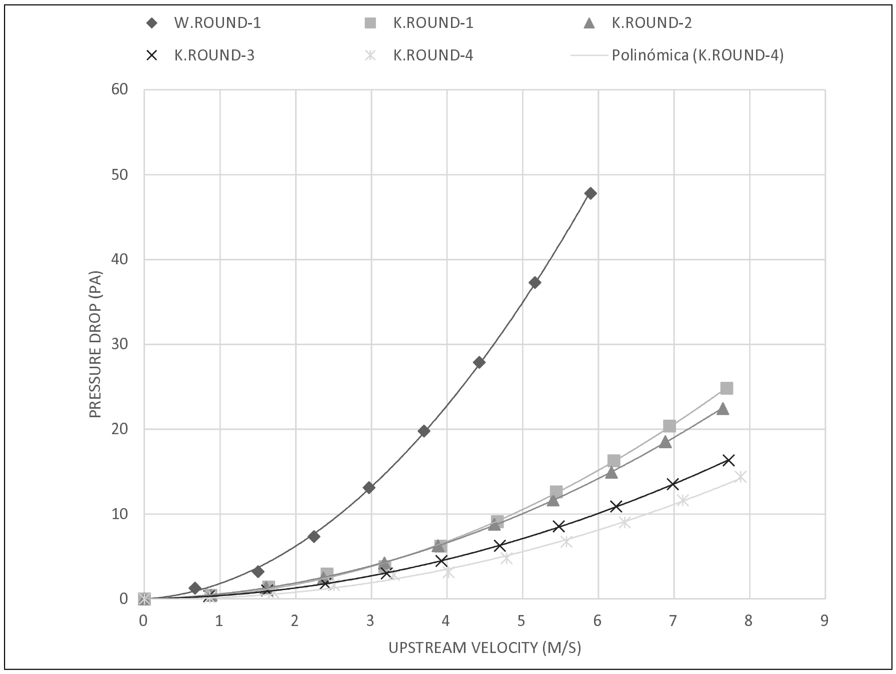

FIGURE 3.6. Pressure drop of the knitted round filament meshes, fitted with equation 3.10

TABLE 3.1. Polynomial fit for all meshes and the theoretical Aerodynamic Collection Efficiency (ACE) calculated with C_0

Ribbon filament type									
			Equation 3.10			Equation 3.11			
Mesh	2R (mm)	Solidity	a	b	R^2	a	R^2	C_0	ACE
K.RIBBON-1	2	0.489	1.45	-0.83	0.9996	1.28	0.9971	2.09	0.21
K.RIBBON-2	2.4	0.383	1.12	-1.27	0.9927	0.89	0.9895	1.47	0.18
K.RIBBON-3	1.7	0.567	1.81	-0.28	0.9991	1.74	0.9989	2.85	0.22
K.RIBBON-4	2	0.574	2.77	-1.52	0.9997	2.34	0.9954	3.84	0.21
K.RIBBON-5	3	0.741	7.85	-2.75	0.9995	6.58	0.9944	10.78	0.19
K.RIBBON-6	2	0.789	13.11	-4.69	0.9998	10.53	0.9916	17.07	0.17
K.RIBBON-7	2.1	0.777	9.25	-2.01	0.9997	8.22	0.9977	13.54	0.18
K.RIBBON-8	1.5	0.777	9.82	-2.48	0.9999	8.54	0.9967	14.04	0.18
K.RIBBON-9	1.8	0.881	20.13	-3.05	0.9983	17.83	0.9961	29.00	0.15
K.RIBBON-10	1.8	0.910	32.39	-3.74	0.9974	25.70	0.9915	47.65	0.21
Round filament type									
			Equation 3.10			Equation 3.11			
Mesh	2R (mm)	Solidity	a	b	R^2	a	R^2	C_0	ACE
W.ROUND-1	0.24	0.603	1.29	0.53	0.9997	1.40	0.9989	2.27	0.25
K.ROUND-1	0.3	0.328	0.42	0.02	0.9991	0.42	0.9991	0.69	0.19
K.ROUND-2	0.3	0.388	0.35	0.24	0.9999	0.39	0.9985	0.65	0.22
K.ROUND-3	0.3	0.336	0.26	0.14	0.9999	0.28	0.999	0.46	0.21
K.ROUND-4	0.3	0.216	0.24	-0.08	0.9967	0.23	0.9963	0.37	0.14

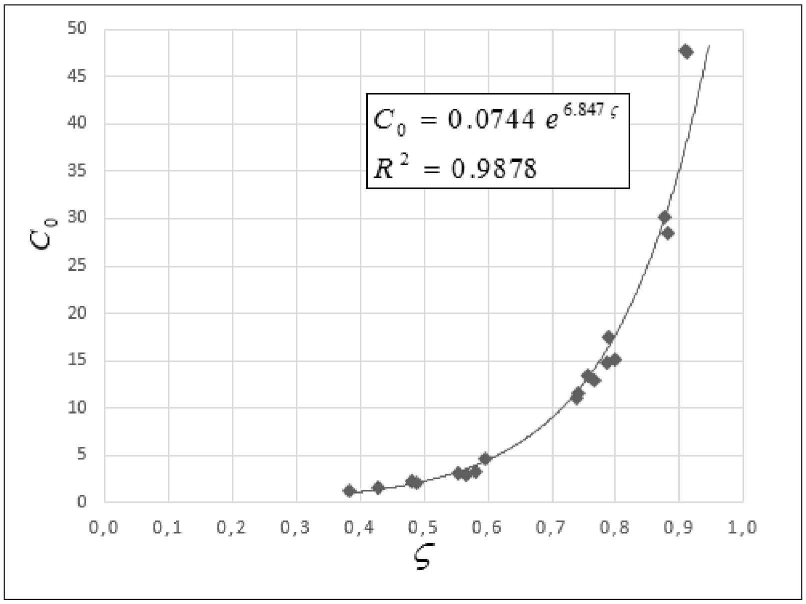

FIGURE 3.7. Relationship between pressure loss coefficient (C_0) and the solidity for knitted ribbon filament type meshes.

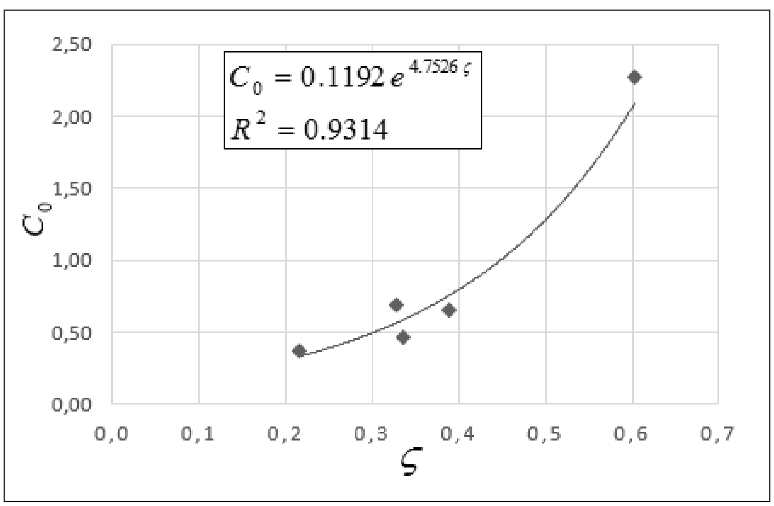

FIGURE 3.8. Relationship between the pressure loss coefficient (C_0) and the solidity for round filament type meshes.

Using equation 3.4 and 3.12, the aerodynamic collection efficiency (ACE) of any mesh can be calculated. Moreover, we can incorporate the deposition efficiency using equations 3.2 and 3.3 ((Park et al.,2013)). However, the Reynolds number in equation 3.3 has to be evaluated at the air velocity just in front of the mesh, u_1, which can be estimated as a function of the unperturbed wind velocity, u_0, following (Rivera,2011):

$$u_1 = \frac{u_0}{1 + \sqrt{\frac{C_0}{C_d}}} \tag{3.13}$$

In summary, knowing the pressure drop coefficient, C_0, as a function of solidity and with the above estimation for the wind velocity in front of the mesh, we can plot the collection efficiency vs. solidity for different wind velocities and for a given droplet diameter distribution. Using the droplet size distribution data of Schemenauer and Joe (1989), Figure 3.9 shows the theoretical collection efficiency as a function of solidity for knitted ribbon meshes, with wind velocity as a parameter, and Figure 3.10 shows the same plots for round filament meshes. Notice that with raising velocities the collection efficiency increases, because the deposition efficiency also increases. The uppermost curve in each figure corresponds to the limit when deposition efficiency is one (one hundred percent), which also represents the ACE. In all cases a collector aspect ratio of 5 was considered that results in C_d=1.2.

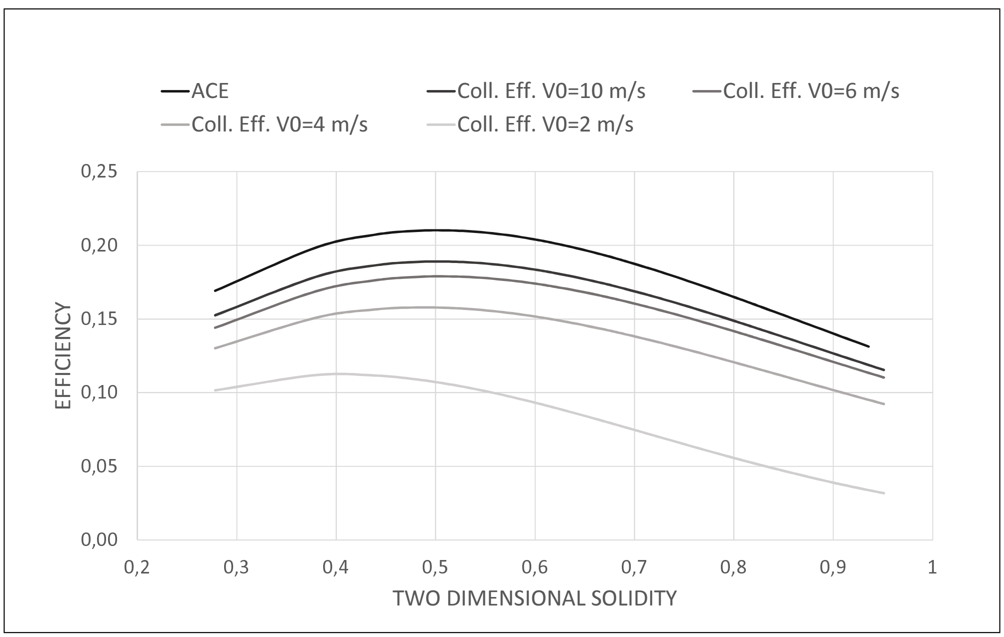

FIGURE 3.9. Theoretical collection efficiency as a function of solidity for a ribbon filament meshes at different unperturbed velocities (u_0) .

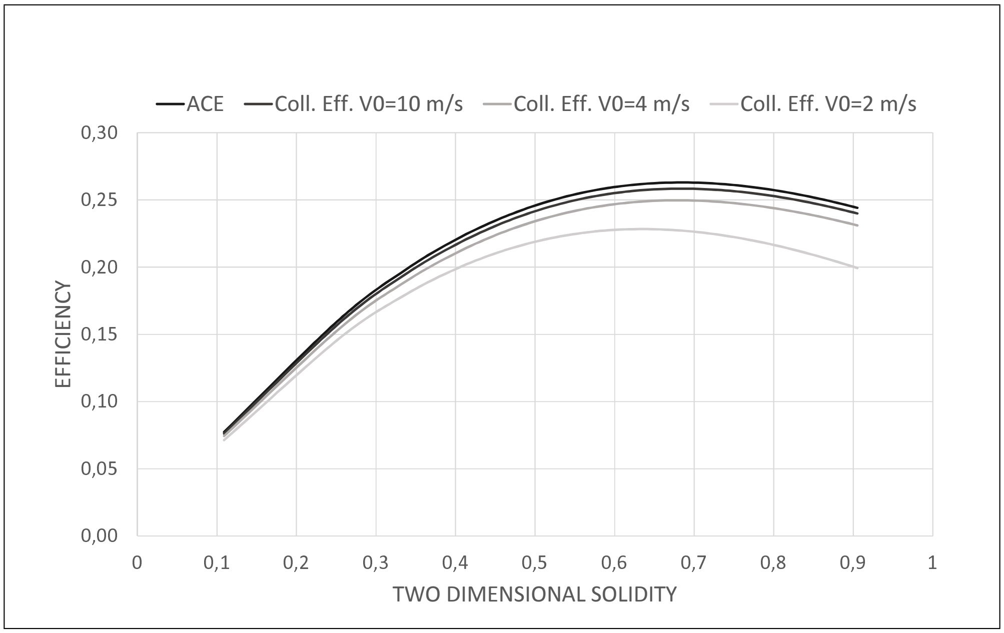

FIGURE 3.10. Theoretical collection efficiency as a function of solidity for round filament meshes at different unperturbed velocities (u_0) .

The top curve of Figure 3.9, which shows the ACE, can be compared to the one presented by (Rivera,2011). The former predicts a maximum ACE of 0.21 at a solidity of 0.502, while the latter gives a maximum ACE of 0.205 at a solidity of 0.55, values surprisingly similar considering that (Rivera,2011) used a correlation for C_0 recommended by Idel'cik (1960) for silk meshes. However, the curves tend to differ for large values of the solidity. Figure 3.10 shows that the collection efficiency of round filament meshes is higher than ribbon type meshes, reaching a maximum ACE of 0.263 for a solidity of 0.68. This is caused by the smaller C_0 and filament diameter of the round filament meshes.

Table 3.2 shows the optimal solidity and theoretical collection efficiency for ribbon and round filament meshes as a function of unperturbed wind velocity.

TABLE 3.2. Optimal solidity and theoretical collection efficiency of ribbon and round filament meshes for different wind velocities

	Ribbon filament mesh		Round filament mesh	
u_o	ς^*	η^*_{coll}	ς^*	η^*_{coll}
2	0.40	0.112	0.63	0.228
4	0.49	0.143	0.66	0.244
6	0.50	0.159	0.66	0.250
10	0.50	0.176	0.67	0.255

4. CONCLUSION

To improve the aerodynamic collection efficiency of a FWC it is neccesary to optimize two parameters: the solidity of the mesh and the pressure loss coefficient of the mesh. The first parameter can be measured accurately with digital image processing by taking a photo of the mesh and counting the pixels corresponding to the mesh (value near 0) and the ones corresponding to the background (value near 255). The measurement error will depend on thread width, but for a thread width less than 1 mm, the expected error should not exceed 3%.

The most important to get accurate results is to discern correctly the silhouette of the mesh, which requires a high contrast between the mesh and the background. For this reason most meshes were photograph on a light table while reflective and white meshes were measured with a black background and front light. Opaque and thick threads meshes can be easily measured while semi-transparent meshes require to extract the usefull part of the image to be measured. Also, solidity of double layer meshes can be measured as simple as a single layer one.

The pressure loss coefficient was measured with a wind tunnel. The presense of inertial flow across the mesh was corroborated with the Reynolds number based on the pore diameter of the mesh and also with the coefficient of determination of a cuadratic polynomial without linear term that was fitted to the data and gave results over 0.99 for most meshes.

Most meshes measured has pore dimension bigger than 1 mm so viscous forces are negligible compared to the inertial, this allows to neglect the effect of the linear term in the polynomial fit, what allows to calculate the pressure loss coefficient as a function of solidity only and independent of Reynolds number.

Relationship between C_0 and solidity for ribbon filament type meshes fitted to an exponential function and the maximum theoretical ACE of this type is 0.2102 for a solidity of 0.503. Round filament type meshes behave locally (between 0.2 and 0.6 solidity) as a polynomial function but an exponential function was fitted to project it behavior at higher solidities, obtaining better ACE than ribbon filament type, reaching a maximum of 0.263 for a solidity of 0.68.

The best ribbon filament mesh, in term of theoretical ACE was the K.RIBBON-3 (solidity: 0.567 ; C_0: 2.85; ACE: 0.223). For the round filament type, the best was the W.ROUND-1 (solidity: 0.603; C_0: 2.27; ACE: 0.254).

The collection efficiency of the mesh is the product of the aerodynamic efficiency and the deposition efficiency. As the last considers the filament width as a critical parameter, round filament meshes has better deposition efficiency than ribbon filament type since it has thinner filaments. Thus the collection efficiency of a round filament mesh is 36 % higher than a ribbon filament mesh at wind velocities of 10 ms^{-1} and at 2 ms^{-1}, collection efficiency of round filament mesh is 123 % higher than ribbon filament mesh.

References

Abdul-Wahab, S., & Lea, V. (2008). Reviewing fog water collection worldwide and in oman. *International Journal of Environmental Studies*, *v. 65*(3), 485498.

Álvarez, A. (2010). *Estudio de las características geométricas y del comportamiento aerodinmico de las mallas antiinsectos utilizadas en los invernaderos como medida de protección vegetal*. Unpublished doctoral dissertation, Almería University.

Álvarez, A., Oliva, R., & Valera, D. (2012). Software for the geometric characterization of insect-proof screens. *Computers Geosciences*, *v. 82*, 134–144.

Antohe, B., & Lage, J. (1997). A general two-equations macroscopic turbulence model for incompressible flow in porous media. *International Journal of Heat and Mass Transfer*, *v. 40*(n. 13), 3013–3024.

Bailey, B., Montero, J., Perez Parra, A., Robertson, A., Baeza, E., & Kamaruddin, R. (2003). Airflow resistance of greenhouse ventilators with and without insect screens. *Biosystem Engineering*, *v. 86*, 217–229.

Boomsma, K., & Poulikakos, D. (2002). The effects of compression and pore size variations on the liquid flow characteristics in metal foams. *Journal of Fluids Engineering*, *v.124*(n.1), 263–272.

Bresci, E. (2002). Wake characterization downstream of a fog collector. *Atmospheric Research*, *v.64*, 217–225.

Castellano, S., & Russo, G. (2005). Reti in plastica per l'agricoltura: modi d'uso, materiali, proprieta fisiche. In *Proceedings of aiia meeting "l'ingegneria agraria per lo sviluppo sostenible dell'area mediterranea.*

Castellano, S., Scarascia, G., Russo, D., Briassoulis, A., Mistriotis, S., Hemming, D., et al. (2008). Plastic nets in agriculture: a general review of types and applications. *Applied Engineering in Agricultural*, *v. 24*, 799–808.

Cereceda, P., Osses, P., Larrain, H., Farías, M., Lagos, M., Pinto, R., et al. (2002). Advective, orographic and radiation fog in the tarapacá region, chile. *Atmospheric Research*, *v.64*, 261–271.

Cohen, S., & Fuchs, M. (1999). Measuring and predicting radiometric properties of reflective shade nets and thermal screens. *Journal of Agricultural Engineering Research*, *v. 73*, 245–255.

Domen, J., Stringfellow, W., Kay, M., & Gulati, S. (2014). Fog water as an alternative and sustainable water resource. *Clean Techn Environ Policy*, *v.16*, 235–249.

Grove, C., & Jerram, D. (2011). An imagej macro to quantify total optical porosity from blue-stained thin sections. *Computer Geosciences*, *v. 37*, 1850–1859.

Guan, D., Zhang, Y., & Zhu, T. (2003). A wind-tunnel study of windbreak drag. *Agricultural and Forest Meteorology*, *v. 118*, 75–84.

Idel'cik, I. (1960). Memento des partes de charge. translation from the russian, original title, spravotchnik po guidravlitcheskim soprotivleniam. *Eyrolles, Paris*.

Kenney, W. (1987). A method for estimating windbreak porosity using digitized photographic silhouettes. *Agricultural and Forest Meteorology*, *v. 39*, 91–94.

Klemm, O., Schemenauer, R. S., Lummerich, A., Cereceda, P., Marzol, V., Corell, D., et al. (2012). Fog as a fresh-water resource: Overview and perspectives. *AMBIO*, *v. 41*, 221–234.

LeBoeuf, R., & Jara, E. De la. (2014). Quantitative goals for large scale fog collection projects as a sustainable freshwater resource in northern chile. *Water International*, *v.39*, 431–450.

Miguel, A., Braak, G. Van de, & Bot. (1997). Analysis of the airflow characteristics of greenhouse screening materials. *Journal of Agricultural Engineering Research*, *v. 67*(n. 1), 105–112.

Molina, F., Valera, D., A.J., A., & Madueno, A. (2006). A wind tunnel study of airflow through horticultural crops: determination of the drag coefficient. *Biosystems Engineering*, *v. 93*, 447–457.

Muñoz, P., Montero, J., Antón, A., & Giufrida, F. (1999). Effecto of insect-proof screens and roof openings on greenhouse ventilation. *Journal of Agricultural Engineering*, *v. 73*, 171–178.

Park, K., Chhatre, S., Srinivasan, R., Cohen, R., & McKinley, G. (2013). Optimal design of permeable fiber network structures for fog harvesting. *Langmuir*, *v. 29*, 13269–13277.

Rivera, J. (2011). Aerodynamic collection efficiency of fog water collectors. *Atmospheric Research*, *v. 102*(n. 3), 335–342.

Schemenauer, R., & Cereceda, P. (1992). Water from fog-covered mountains. *Waterlines*, *v. 10*(n. 4).

Schemenauer, R., & Joe, P. (1989). The collection efficiency of a massive fog collector. *Atmospheric Research*, *v. 24*, 53–69.

Teitel, M., Dvorkin, D., Haim, Y., Tanny, I., & Seginer. (2009). Comparison of measured and simulated flow through screens: effects of screen inclination and porosity. *Biosystems Engineering*, *v. 104*, 404–416.

Valera, D., Alvarez, A., & Molina, F. (2006). Aerodynamic analysis of several insect-proof screens used in greenhouses. *Spanish Journal of Agricultural Research*, *v. 4*, 273–279.

Appendix

APPENDIX A. WIND TUNNEL DIMENSIONS

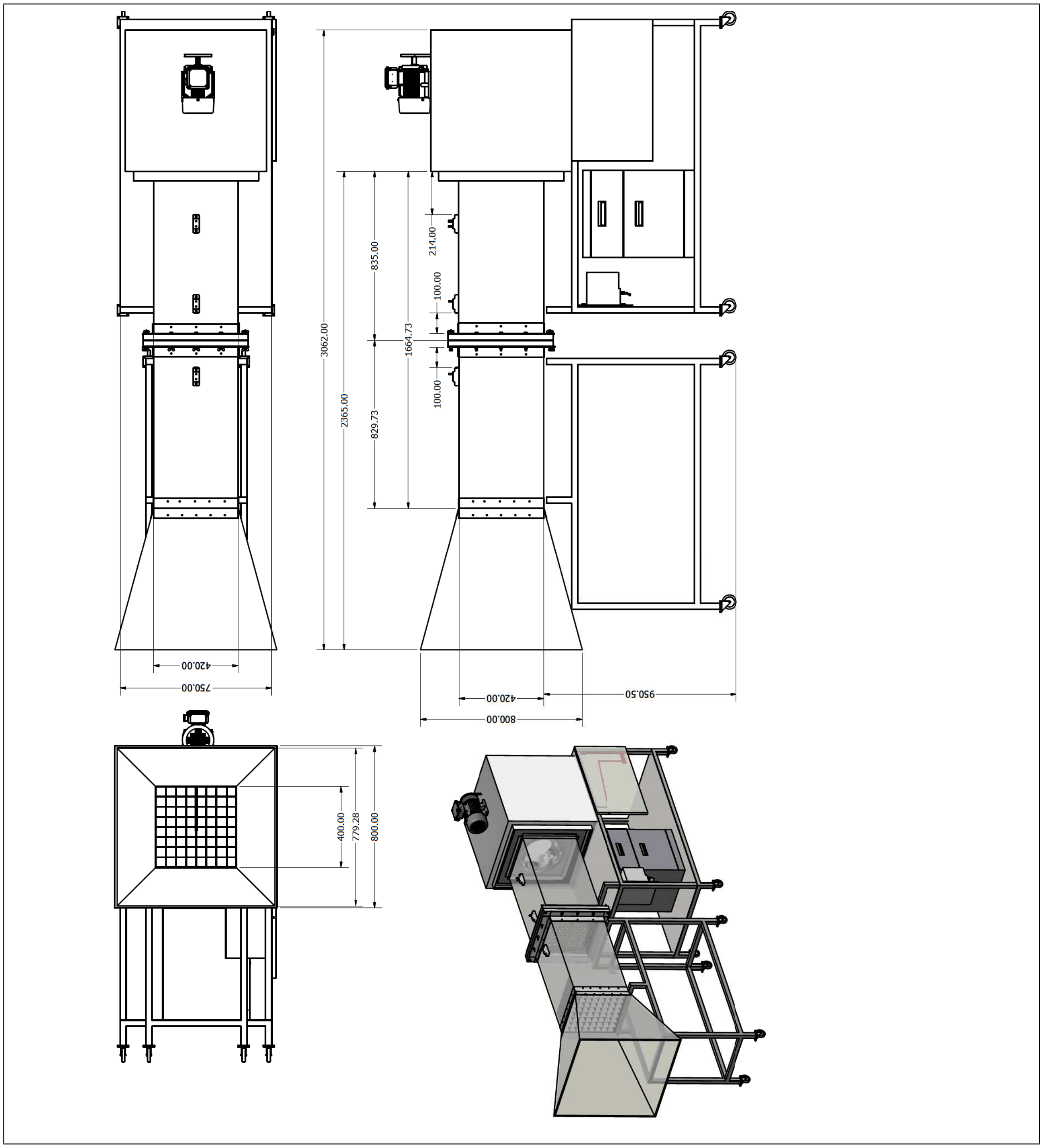

FIGURE A.1. Wind tunnel dimensions

APPENDIX B. CENTRIFUGAL AIR INTAKE FAN

The wind tunnel is equipped with an exhaust fan CLT-15 (Soler Palau, Santiago, Chile) which has an impeller with straight blades delayed. Figure B.1 shows the main parts of the fan. On the other hand, figure B.2 shows the main features of the fan and figure B.3 shows the charasteristic curve.

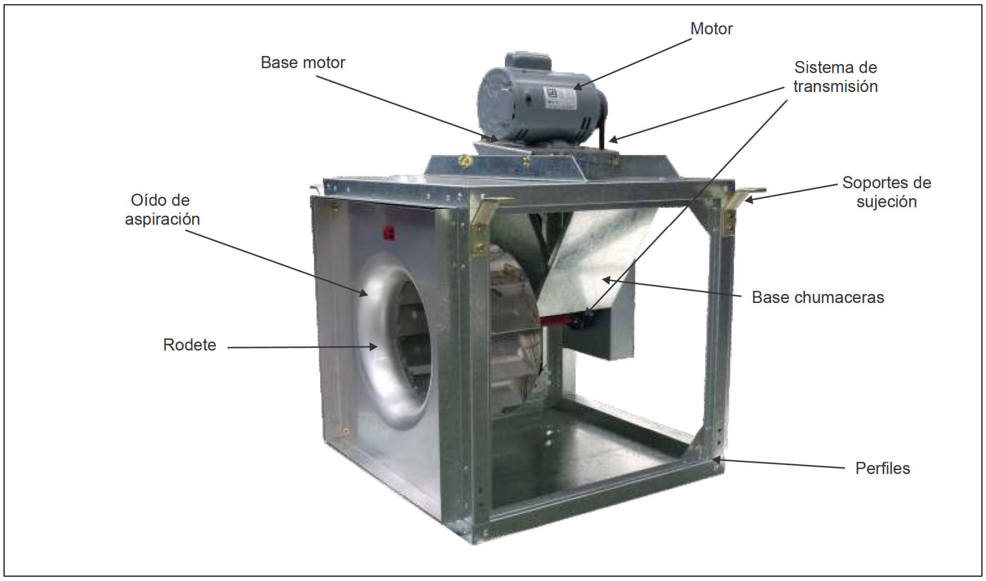

FIGURE B.1. Centrifugal Fan used in the wind tunnel

B.1. Fan sizing

To select the appropiate fan for the wind tunnel, it is neccesary to estimate the pressure loss along the installation.

Considering the main parts of the wind tunnel, pressure losses will occur in:

(i) Tunnel walls
(ii) Flow straightener

CLT 15

CARACTERÍSTICAS PRINCIPALES

Diámetro de la turbina: 401 mm. (15 13/16 inch).
Diámetro del eje: 22.22 mm. (7/8 inch).
Área de salida: 0.372 m^2 (4.004 ft^2).
BHP máximos: 3.20
Armazón máximo de motor: 184 T
RPM máximas: 2130
Peso del equipo: 54 Kg (118 Lb).

HP	RPM	PRESIÓN ESTÁTICA mmca-inwg																							
		3.17mm/0.125"		6.35 mm/0.250"		12.70mm/0.500"		19.05mm/0.750"		25.40mm/1.000"		31.75mm/1.250"		38.1mm/1.500"		44.45mm/1.750"		50.8mm/2.000"		63.50mm/2.500"		69.85mm/2.750"		76.2mm/3.000"	
		CFM	BHP	CFM	BHP	CFM	BHP	CFM	BHP	CFM	BHP	CFM	BHP	CFM	BHP	CFM	BHP	CFM	BHP	CFM	BHP	CFM	BHP	CFM	BHP
		m^3/hr	dB(A)	m^3/hr	dB(A)	m^3/hr	dB(A)	m^3/hr	dB(A)	m^3/hr	dB(A)	m^3/hr	dB(A)	m^3/hr	dB(A)	m^3/hr	dB(A)	m^3/hr	dB(A)	m^3/hr	dB(A)	m^3/hr	dB(A)	m^3/hr	dB(A)
1/4	790	1635	0.16	1375	0.16																				
		2777	59	2336	57																				
	857	1817	0.20	1577	0.21																				
		3087	61	2679	59																				
1/3	924	1996	0.25	1773	0.26	1279	0.26																		
		3391	62	3012	60	2173	57																		
	991	2174	0.31	1963	0.32	1530	0.32																		
		3694	64	3335	62	2599	58																		
1/2	1058	2351	0.38	2149	0.39	1756	0.39	1231	0.37																
		3994	65	3651	63	2983	60	2092	57																
	1125	2526	0.45	2334	0.46	1968	0.47	1540	0.46																
		4292	66	3965	65	3343	61	2617	59																
3/4	1192	2701	0.54	2515	0.55	2171	0.56	1797	0.56	1247	0.51														
		4588	68	4273	66	3688	62	3052	60	2119	56														
	1259	2874	0.63	2695	0.64	2369	0.66	2029	0.66	1605	0.64														
		4883	69	4579	67	4025	63	3448	61	2727	57														
1	1326	3046	0.74	2874	0.75	2562	0.76	2247	0.77	1886	0.76	1350	0.70												
		5175	70	4883	68	4352	64	3818	62	3204	59	2293	57												
	1393	3218	0.86	3052	0.87	2752	0.88	2457	0.89	2134	0.89	1726	0.86												
		5468	71	5185	69	4676	66	4174	63	3626	60	2932	58												
	1460	3390	0.99	3228	1.00	2939	1.01	2660	1.03	2363	1.03	2019	1.01	1529	0.94										
		5760	72	5485	70	4993	67	4519	64	4015	61	3430	59	2597	57										
1 1/2	1527	3561	1.13	3405	1.14	3125	1.16	2857	1.17	2582	1.18	2277	1.17	1896	1.13	1230	0.98								
		6051	73	5785	71	5309	68	4854	65	4387	62	3868	60	3221	58	2090	55								
	1594	3732	1.28	3580	1.29	3308	1.31	3052	1.33	2792	1.34	2513	1.34	2190	1.31	1757	1.24								
		6341	74	6082	72	5621	68	5185	66	4743	63	4269	61	3721	59	2985	56								
	1661	3902	1.45	3754	1.46	3491	1.48	3243	1.50	2996	1.51	2737	1.51	2450	1.50	2102	1.46	1587	1.34						
		6630	75	6378	73	5931	68	5510	67	5090	63	4650	61	4162	60	3572	56	2696	54						
2	1728	4072	1.63	3928	1.64	3671	1.66	3431	1.68	3195	1.70	2953	1.71	2690	1.70	2391	1.67	2012	1.61						
		6918	76	6674	74	6237	69	5830	68	5429	64	5016	62	4571	61	4062	57	3419	55						
	1795	4242	1.83	4102	1.84	3851	1.86	3618	1.88	3392	1.90	3161	1.91	2917	1.91	2649	1.90	2335	1.85						
		7207	77	6969	75	6543	70	6148	69	5762	65	5371	63	4956	62	4501	58	3967	56						
3	1862	4412	2.04	4274	2.05	4030	2.07	3804	2.10	3585	2.12	3364	2.13	3136	2.13	2890	2.13	2615	2.10	1813	1.90				
		7496	77	7261	76	6847	71	6463	70	6091	66	5716	64	5328	62	4910	59	4443	57	3080	54				
	1929	4581	2.27	4447	2.28	4208	2.30	3988	2.33	3776	2.35	3564	2.36	3347	2.37	3119	2.37	2869	2.35	2233	2.23	1699	2.04		
		7782	78	7556	76	7149	72	6775	70	6415	67	6055	65	5687	63	5299	60	4875	57	3794	55	2886	53		
	1962	4664	2.38	4532	2.40	4296	2.42	4078	2.45	3869	2.47	3662	2.49	3450	2.50	3227	2.50	2989	2.48	2403	2.38	1969	2.25		
		7924	79	7699	77	7298	73	6928	71	6574	67	6221	65	5861	64	5483	60	5078	58	4083	55	3345	54		
	1996	4749	2.51	4618	2.52	4386	2.55	4170	2.57	3965	2.60	3761	2.61	3553	2.63	3338	2.63	3109	2.62	2563	2.54	2189	2.43	1571	2.18
		8069	79	7846	77	7451	73	7085	71	6736	67	6390	65	6037	64	5671	60	5282	58	4354	56	3719	54	2669	52
	2063	4918	2.77	4790	2.78	4562	2.81	4353	2.84	4152	2.86	3955	2.88	3755	2.90	3551	2.90	3337	2.90	2848	2.85	2546	2.78	2150	2.65
		8356	80	8139	78	7751	74	7395	72	7054	68	6719	66	6380	65	6033	61	5669	59	4838	56	4325	55	3653	52
5	2130	5086	3.05	4961	3.06	4738	3.09	4533	3.12	4338	3.14	4146	3.16	3955	3.18	3759	3.19	3557	3.20	3110	3.16	2848	3.11	2535	3.03
		8640	80	8429	79	8050	75	7701	73	7370	69	7044	67	6719	65	6386	62	6043	60	5284	57	4838	55	4308	53

FIGURE B.2. Fan features.

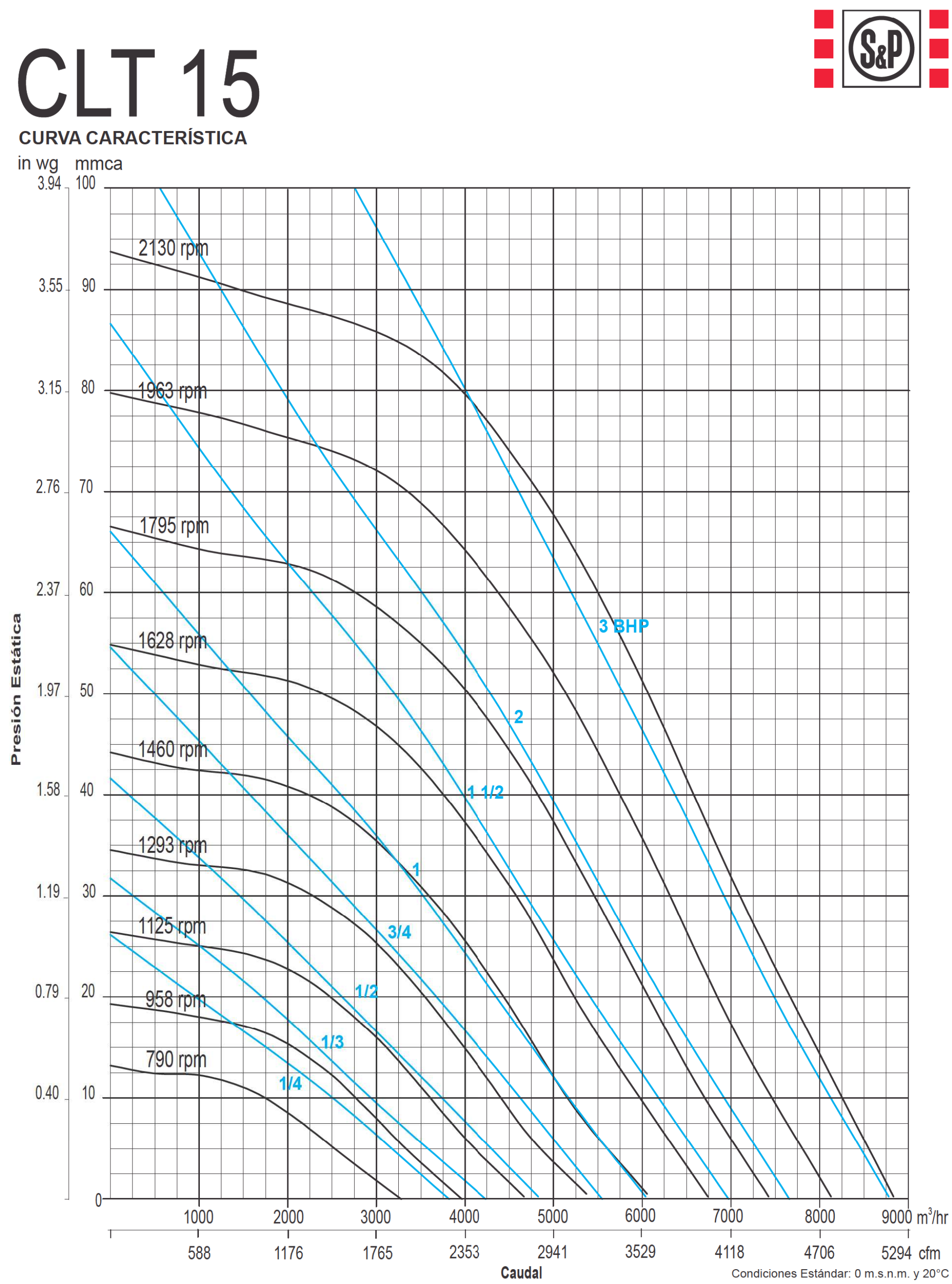

FIGURE B.3. Charasteristic curve of the fan.

(iii) Mesh

(iv) Singular losses

B.1.0.1. Tunnel walls

On tunnel walls there will be pressure losses due to the friction between air and walls. Thus, pressure losses will depend on the length of the tunnel, on the cross section and the material.

To calculate these losses the Darcy-Weisbach equation was used

$$\Delta P_f = f(\frac{L}{D})\rho\frac{V^2}{2} \tag{B.1}$$

Where:

ΔP_f: pressure loss due to friction.

f: friction factor, which depends on walls material.

L: tunnel length.

ρ: density of air.

V: wind velocity.

D: hidraulic diameter of the tunnel, which for square cross section is $\frac{4A}{P}$ where A is the cross sectional area and P is the perimeter.

Calculating the Reynolds number, it is possible to determine the type of flow in the interior of the wind tunnel and thus determine the friction factor f.

$$R_e = \frac{U \cdot D_h}{\nu} \tag{B.2}$$

Considering a square section of 0.4 m side and a viscosity of air (ν) equal to $1,85 \cdot 10^{-5}[\frac{N \cdot s}{m^2}]$, Reynolds number was calculated for wind velocities between 0 and 10 ms^{-1}

Table B.1shows the Reynolds number for different wind velocities.

TABLE B.1. Reynolds number for different wind velocities

U (ms^{-1})	Reynolds
0	0
1	21622
2	43243
3	64865
4	86486
5	108108
6	129730
7	151351
8	172973
9	194595
10	216216

It can be seen that the flow inside the tunnel will be turbulent always. Thus the friction factor will be determined by

$$f = [-2 \cdot \log(\frac{\epsilon}{3.7 \cdot D_h})]^{-2} \tag{B.3}$$

Where ϵ corresponds to the absolute roughness of the walls.

Considering that tunnel walls are made of acrylic, we used a value of $\epsilon = 0.015mm$. Evaluating for $\epsilon = 1.5 \cdot 10^{-5}m$ and $D_h = 0.4m$ we obtained a value of $f = 0.01$

Thus, friction losses are:

$$\Delta P_f = 0.01 \cdot (\frac{2}{0.4}) \cdot 1.2 \cdot \frac{U^2}{2} \tag{B.4}$$

Table B.2 shows the friction losses as a function of wind velocity.

TABLE B.2. Pressure loss on the tunnel walls as a function of wind velocity.

U (ms^{-1})	$\Delta P_f (mm.w.c)$
0	0.000
1	0.003
2	0.012
3	0.028
4	0.049
5	0.077
6	0.110
7	0.150
8	0.196
9	0.248
10	0.307

B.1.0.2. Flow straightener

The ASHRAE equation was used to estimate the pressure loss due to the flow straightener

$$\Delta P_j = C \cdot \rho \cdot \frac{U^2}{2}, \tag{B.5}$$

where C corresponds to an adimensional value gived by the fractional uncovered area of the flow straightener.

For the flow straightener used in the wind tunnel, it was calculated a fractional uncovered area of 93,31%, which corresponds to a value of $C = 0.1$ (see table B.3).

TABLE B.3. Pressure loss factor gived by ASHRAE

Pressure loss due to flow straightener	
Fractional uncovered area	C
0.3	6.2
0.4	3
0.5	1.65
0.6	0.97
0.7	0.58
0.8	0.32
0.9	0.14

Thus, the pressure loss due to the flow straightener is

$$\Delta P_j = 0.1 \cdot 1.2 \cdot \frac{U^2}{2}. \tag{B.6}$$

Table B.4 shows the pressure loss of the flow straightener as a function of wind velocity inside the wind tunnel.

TABLE B.4. Pressure loss due to the flow straightener as a function of wind velocity

U (ms^{-1})	$\Delta P_j (mm.w.c)$
0	0
1	0.006
2	0.024
3	0.055
4	0.098
5	0.153
6	0.220
7	0.300
8	0.391
9	0.495
10	0.612

B.1.0.3. Mesh

When the airflow passes through the mesh, which is perpendicular to the flow direction, an important pressure loss is produced and it depends on the solidity of the mesh.

Pressure loss due to the mesh is given by

$$\Delta P_m = C_0 \cdot \rho \cdot \frac{U^2}{2}, \tag{B.7}$$

where C_0 is the pressure loss coefficient.

Taking as a reference the Raschel mesh, we used the Idel'cik correlation for silk meshes:

$$C_0 = 1.62(1.3\varsigma + (\frac{\varsigma}{1-\varsigma})^2), \tag{B.8}$$

where ς is the solidity of the mesh.

Assuming that we will use meshes with solidities up to 0.7, the pressure losses were calculated with $\varsigma = 0.7$.

Table B.5 shows the pressure loss for a Raschel mesh with $\varsigma = 0.7$ as a function of wind velocity.

TABLE B.5. Pressure loss due to a silk mesh of solidity $\varsigma = 0.7$ as a function of wind velocity.

U (ms^{-1})	$\Delta P_m(mm.w.c)$
0	0.0
1	0.5
2	2.1
3	4.7
4	8.4
5	13.1
6	18.9
7	25.7
8	33.6
9	42.5
10	52.5

B.1.0.4. Singular losses

Since the centrifugal fan sucks the air, the airflow will enter from the diffuser, located at the entrance of the tunnel. On the moment that flows enter the tunnel, a pressure loss is produced given by

$$\Delta P_s = k \cdot \rho \cdot \frac{U^2}{2}, \tag{B.9}$$

where k is a factor that depends on the type of entrance of the tunnel. For the designed entrance, a k=0.78 value was considered so the singular losses are given by

$$\Delta P_s = 0.78 \cdot 1,2 \cdot \frac{U^2}{2}. \tag{B.10}$$

Table B.6 shows the singular losses as a function of wind velocity.

TABLE B.6. Singular pressure loss as a function of wind velocity

U (m/s)	$\Delta P_s (mm.w.c)$
0	0.00
1	0.05
2	0.19
3	0.43
4	0.76
5	1.19
6	1.72
7	2.34
8	3.05
9	3.86
10	4.77

B.1.0.5. Total pressure loss

Total pressure loss of the system is given by

$$\Delta P_t = \Delta P_f + \Delta P_j + \Delta P_m + \Delta P_s. \tag{B.11}$$

Table B.7 shows the total pressure loss as a function of wind velocity.

TABLE B.7. Total pressure loss of the system as a function of wind velocity

U (m/s)	ΔP_f (mm.w.c)	ΔP_j (mm.w.c)	ΔP_m (mm.w.c)	ΔP_s (mm.w.c)	ΔP_t (mm.w.c)
0	0.000	0.000	0.000	0.000	0.0
1	0.003	0.006	0.525	0.048	0.6
2	0.012	0.024	2.099	0.191	2.3
3	0.028	0.055	4.722	0.429	5.2
4	0.049	0.098	8.395	0.763	9.3
5	0.077	0.153	13.117	1.193	14.5
6	0.110	0.220	18.888	1.717	20.9
7	0.150	0.300	25.709	2.338	28.5
8	0.196	0.391	33.579	3.053	37.2
9	0.248	0.495	42.499	3.864	47.1
10	0.307	0.612	52.468	4.771	58.2
11	0.371	0.740	63.486	5.772	70.4
12	0.441	0.881	75.554	6.870	83.7
13	0.518	1.034	88.671	8.062	98.3
14	0.601	1.199	102.837	9.350	114.0
15	0.690	1.376	118.053	10.734	130.9

Due to the high pressures required, we decided to use a centrifugal type exhaust fan with impeller of plane delayed blades.

Thus, intercepting the charasteristic curve of the selected fan and the charasteristic curve of the wind tunnel resistance, the work point can be found.

Using this fan, we can reach velocities of about 7 ms^{-1} inside the tunnel with a mesh of 0.7 solidity. This situation is plotted in figure B.4.

On the other hand, using a Raschel 35% SC mesh, we expect velocities of 9 ms^{-1}. This situation is plotted in figure B.5.

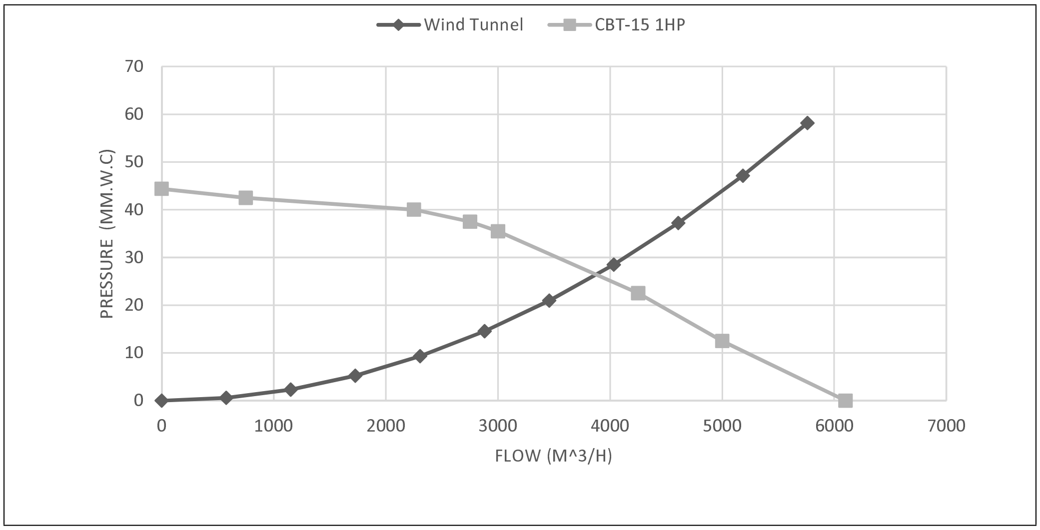

FIGURE B.4. Work point for a 0.7 solidity mesh.

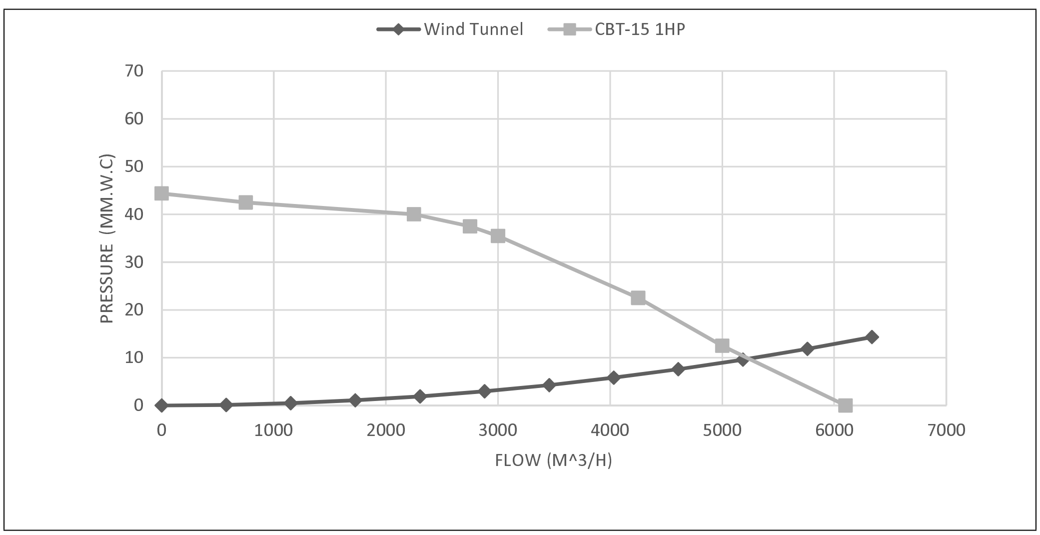

FIGURE B.5. Work point for a mesh of 0.35 solidity.

APPENDIX C. PARTS OF THE WIND TUNNEL DESIGN

C.1. Testing framework

This part of the wind tunnel allows to test different meshes. It consists of two frames made of stainless steel which allows to fix the mesh. This process can be done outside the wind tunnel. Figure C.1 shows how to fix the mesh.

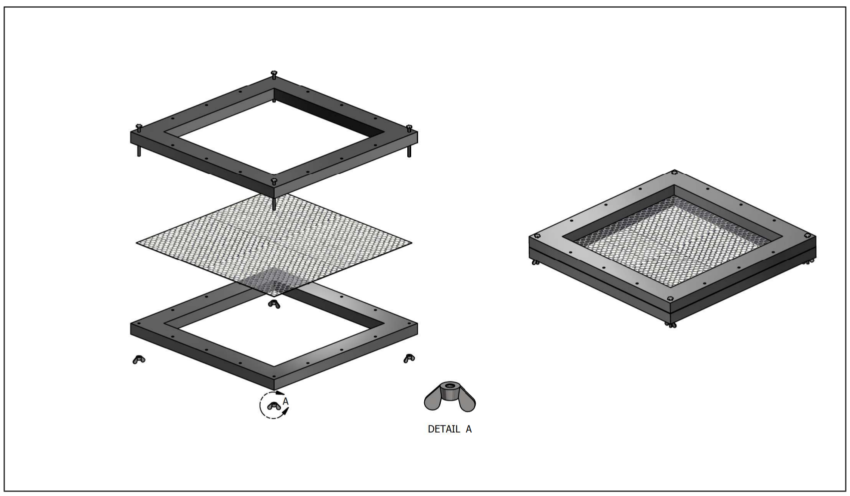

FIGURE C.1. Mesh assembled on the testing framework.

Once the mesh has been assembled, the testing framework has to be fixed to the wind tunnel. Figure C.2 shows how to fix the framework on the wind tunnel.

C.2. Pitot tube

To measure wind velocity inside the wind tunnel, a type s Pitot tube was used, because it is easy to make and highly accurate when it is well calibrated. Figure C.3 shows the operation of the instrument. It can be

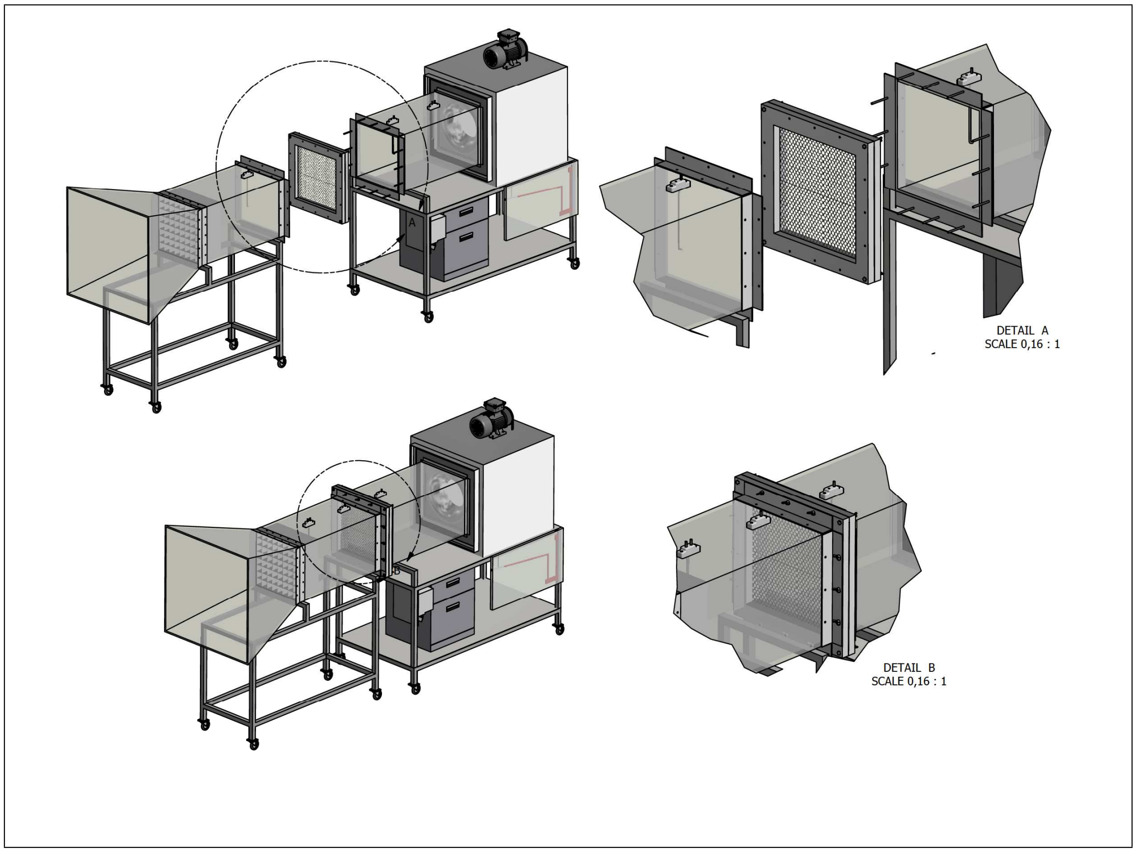

FIGURE C.2. Testing framework assembled on the wind tunnel

seen that the Pitot tube consists of two tubes, the left one is open to the airflow therefore it measures total pressure of the flow (P_t), while right tube is not open to the airflow, therefore it measures static pressure (P_s). Then, the difference between these pressures corresponds to the dynamic pressure (P_d).

The hosepipe with fluid inside of figure C.3 has been drawn just to illustrate the concept of measurement, because the tubes are actually connected to a differential pressure sensor.

To measure wind velocity as a function of the dynamic pressure, the following equation was used:

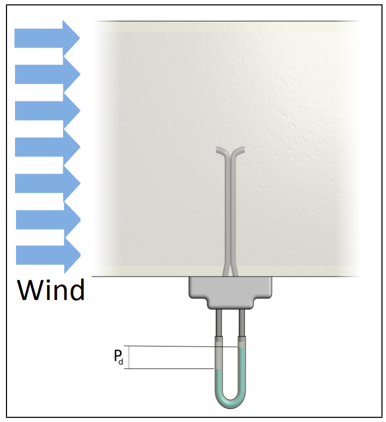

FIGURE C.3. Type s Pitot tube

$$u = \sqrt{\frac{2 \cdot P_d}{\rho}} \tag{C.1}$$

C.3. Differential pressure meter

To measure the pressure loss across the mesh, two tubes were used, where one was placed upstream and the other downstream the mesh to measure static pressure at both sides. Then pressure loss was calculated with the pressure difference. Figure C.4 shows the operation of the pressure loss meter, where the hosepipe with fluid has been drawn to illustrate the concept, because the tubes are actually connected to a differential pressure sensor.

C.4. Differential pressure sensor

The operating principle of the differential pressure sensor (DPS) is a heater placed between two thermopile that heats both equally, but when a flow passes through it, the thermopile placed downstream is heated more than the one placed upstream. Then, the temperature difference between two

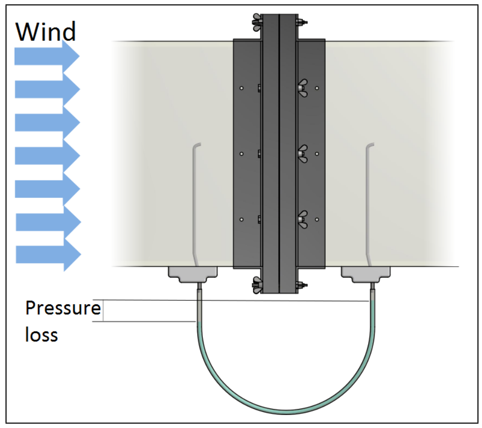

FIGURE C.4. Pressure loss meter

thermopiles is approximately proportional to square root of the mass flow across the sensor chip. Its mass flow sensing and output sensivity depends on gas composition. Figure C.5 shows the sensor operation.

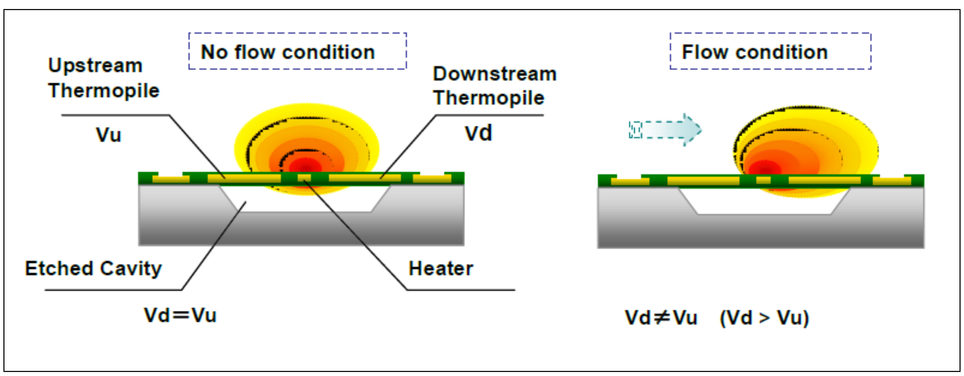

FIGURE C.5. Operating principle of DPS.

Figure C.6 shows the DPS used in the wind tunnel. Sensor 1 has their terminals connected to the Pitot tube and it can measures in the range 0-250 Pa. Sensor 2 is connected to the pressure loss meter and it can measures in the range -50 to 50 Pa.

To analyze the data collected by the d.p.s. it is necessary to read it on the computer. For this purpose, the hardware used was Arduino Uno and

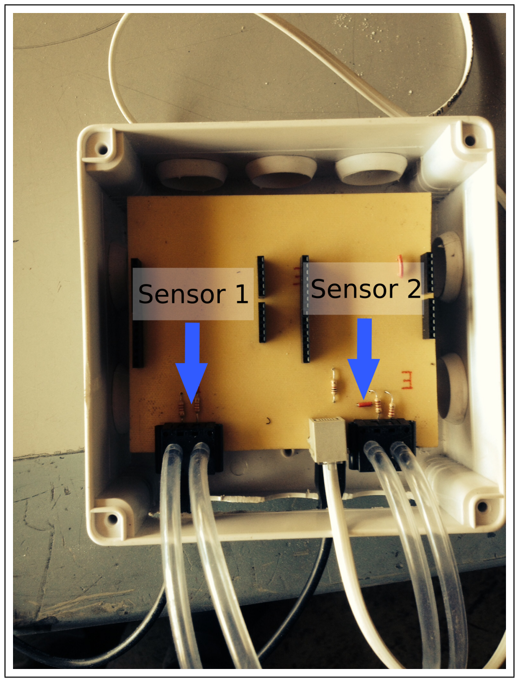

FIGURE C.6. DPS used in the wind tunnel.

we programmed a code to see the sensor read every 0.5 seconds. The sensor read is not the pressure difference but is an adimensional number that can be calibrated to give the pressure difference in a specific unity. For the case of the d.p.s connected to the Pitot tube, calibration were done using a hot wire anemometer, and for the d.p.s connected to the pressure loss meter, calibration were done using an inclined water column manometer.

C.5. Variable frecuency drive

The variable frecuency drive (VFD) can replace the 3-phase motor starter to operate the fan at variable speed. Since the fan can be operated at any speed below its maximum, airflow can be varied by controlling the motor speed instead of the air inlet damper. The VFD used in the wind tunnel was the ABB ACS150, which can vary the frecuency between 0 and 50 Hz. Figure C.7 shows the VFD installed on the wind tunnel.

FIGURE C.7. Variable frecuency drive